Michel Lefebvre
Anotad Copy.

RD3 note 41
January 28, 1993

Electromagnetic Liquid Argon Accordion Calorimeter Simulation

PART I

Michel Lefebvre
University of Victoria, British Columbia, Canada

Gaston Parrour, Pierre Pétroff
LAL, Orsay, France

Abstract

Monte Carlo simulation results on the cartesian and cylindrical accordion electromagnetic calorimeters are presented. The 1992 pointing geometry is also introduced.

Contents

1 Introduction

In order to achieve fast and hermetic liquid argon (LAr) calorimetry for the LHC, the RD3 collaboration [1] proposed a novel accordion structure. Prototypes were built and tested. A cartesian geometry electromagnetic (EM) prototype was tested in 1990 [2] and 1991 [3]. Another small EM prototype, this time with cylindrical geometries, was tested in 1991 [4]. A large pointing geometry EM and hadronic calorimeter prototype is currently under tests.

Since the very beginning of these activities, computer simulations have played a crucial role in guiding and optimising the prototypes' geometrical parameters, as well as in providing some understanding of the experimental results. An initial effort, reported in [5], showed that the uniformity of response of the accordion EM calorimeter could be optimised by minimising the variations of the LAr traversed for various normal incidence impact points. Detailed charge collection was also simulated and its effect found to be small.

Since then the simulation effort has intensified enormously, in phase with the tests of new prototypes. Charge collection simulation has been rewritten and larger data samples have been produced, revealing effects confirmed by experiments; cylindrical and pointing geometries have been and are still simulated in great details.

This note is an attempt to summarise some of the results obtained for the cartesian and cylindrical geometries in the past two years. After a brief word on the software and platforms used, chapter 3 describes the charge collection simulation method followed. Simulation results, often including charge collection simulation and comparison with data, are reported in the following two chapters: chapter 4 for the cartesian geometry (where charge collection simulation is less important) and chapter 5 for the cylindrical (opening and compensated) geometries (where charge collection simulation is more important). A brief introduction to current simulation activities on the pointing geometry EM calorimeter can be found in chapter 6. More on this subject will be presented in a subsequent note.

2 Software Environment

The Monte Carlo simulation described in this note is based on the GEANT simulation package.

A part of the simulation computation has been performed with a farm of HP 9000 computers (BASTA station) at the IN2P3 computing center at Lyon. The Basta station consists in 2 HP 9000 type 730 and 3 HP 9000 type 720. The 720 model is roughly equivalent in time to 3090 IBM processor, while the 730 model is 20% faster. Results are stored in a 200 Mbytes temporary disk then transferred to IBM to be registered on 200 Mbytes cartridges.

Simulations were also performed on a 4cpu 64Mbytes Apollo DN10000 in Victoria, British Columbia, Canada.

3 Charge Collection Simulation

For each charged track segment GEANT provides the starting point, the direction, the length, the associated deposited energy, etc. A set of such quantities for each segment is called a 'hit'. In particular in LAr each secondary particle, electrons or photons, is tracked down a cutoff (10 keV for both) and corresponding hits are recorded in a bank. Using hits the readout current corresponding to drifting charges in the LAr can be determined. When charge collection simulation is performed, the method described below is used.

3.1 Signal Induced by Drift Charges and Readout Electronics

3.1.1 signal

case of a single charge The instantaneous current produced by a charge q_0, at position $\vec{r}$ at time t, and which is drifting is given by

$$i(t) = \frac{q_0}{V_0} \vec{E} \cdot \vec{v} \tag{1}$$

where V_0 is the voltage applied between ground and the positive electrode, $\vec{E}$ is the electric field at $\vec{r}$, $\vec{v}$ is the drift velocity $\vec{v} = \vec{v}(|\vec{E}|)$.

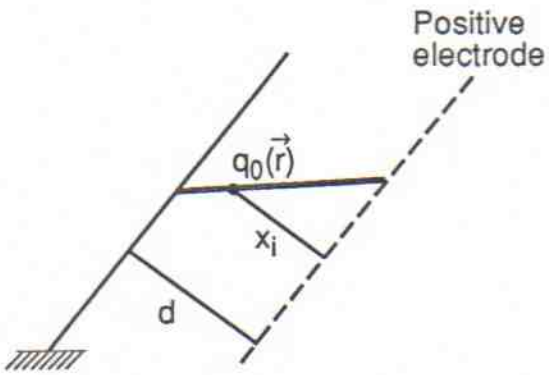

The collected charge q_c, until q_0 reaches the electrode, is:

$$q_c = \frac{q_0}{V_0} \int_0^{t_D} \vec{E} \cdot \vec{v} dt$$

where t_D is the corresponding drift time. Therefore

$$q_c = \frac{q_0}{V_0} \int \vec{E} \cdot d\vec{\ell} = \frac{q_0}{V_0} V \tag{2}$$

where V is the voltage between the initial charge position and the electrode.

example: case of a uniform electric field $\vec{E}$ In this case equipotentials are equidistant. That means

$$V = V_0 \frac{x}{d} ,$$

where d is the gap width and x the distance to the positive electrode. Therefore

$$q_c = q_0 \frac{x}{d} . \tag{3}$$

A continuous charged line in the gap (a hit obtained from simulation) carrying a charge Q_0 is then divided into N equal subsegments with equal charge $\delta Q_0 = Q_0/N$ (assuming uniform ionisation along the line).

The collected charge for such a subsegment at a mean distance x_i from the electrode is

$$\delta Q_c = \delta Q_0 \frac{x_i}{d} = \frac{Q_0}{N} \frac{x_i}{d} .$$

And the total collected charge is

$$Q_c = \sum_{i=1}^{N} \frac{Q_0}{N} \frac{x_i}{d} = \frac{Q_0}{d} \frac{1}{N} \sum_{i=1}^{N} x_i$$

and in the limit $N \to \infty$, $Q_c = Q_0/2$.

In this case of uniform electric field, the collected charge Q_c is half the hit charge Q_0.

Formula (1) shows that $i(t)$ is constant in this case until the elementary charge reaches the electrode. The drift time is $t_D^i = x_i/v$. So for a hit, i.e. a uniform charged track in a gap d, the drifting of charges yields a total current $I(t)$ with a typical triangular shape:

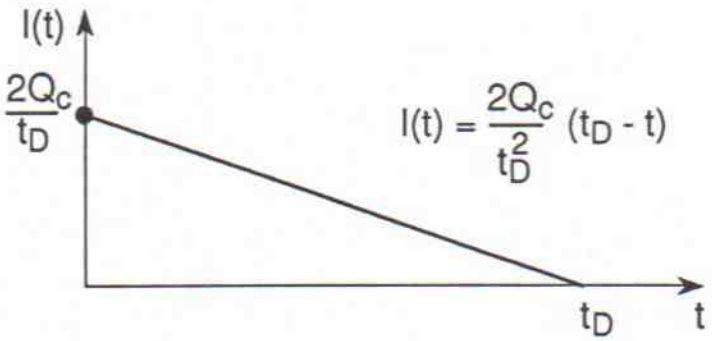

$(t_D = d/v)$

In a more general variable electric field, Eqs. (1) and (2) only are valid. To obtain $I(t)$ distribution, or any quantities related to drift charges, a numerical integration is necessary.

3.1.2 readout electronics

aims To obtain the energy of the primary particle it is necessary to measure the energy deposited by the shower which is related to charges associated to hits. These are linked to the collected charges ($Q_c = Q_0/2$ in case of a uniform $\vec{E}$ field). So the current $I(t)$ is integrated in a charge preamplifier.

To improve the signal to noise ratio (including the pile-up noise), this charge preamplifier is followed by a filter. In the present case of high counting rate, a bipolar filter is foreseen.

bipolar filter Such a filter consists of two derivatives followed by n integrations. It is labelled $(CR)^2\ (RC)^n$.

The choice for n is dictated by noise considerations (especially pile-up at high counting rate). Present values are either $n = 3$ or $n = 4$.

impulse response The impulse response of the whole system (charge integrator + filter), which is also the step response of the filter alone, has the following shape

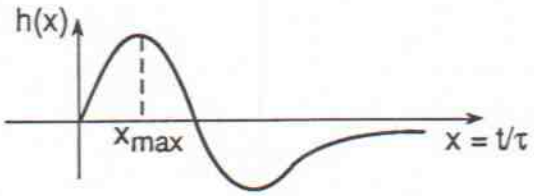

with $\int_0^\infty h(x)dx = 0$, and

$$h(x) = \frac{(n+1-x)x^n}{(n+1)!}e^{-x} \tag{4}$$

$x = t/\tau$, τ the time constant RC. Hereafter $h(t/\tau) = g(t)$.

The maximum value for $h(x)$ is for:

$$x_{\max} = \frac{t_\delta}{\tau} = n + 1 - \sqrt{n+1} \tag{5}$$

t_δ is referenced as "the peaking time for a δ-Dirac function at the entrance of the whole system".

3.2 Output Signal from the Detector

3.2.1 response to a current function $I(t)$ at the entrance

The effective collected current is then

$$I_{\text{eff}}(t) = I(t) \otimes g(t)$$
$$I_{\text{eff}}(t) = \int_o^t I(t')g(t-t')dt' \tag{6}$$

as $I(t')$ is defined for $t' \geq 0$.

3.2.2 case of a uniform electric field

In this case $I(t')$ has the typical triangular shape, and a direct calculation of I_{eff} from (6) is straightforward. This opportunity is used in the simulation for all parts of the apparatus where $\vec{E}$ is uniform and saves CPU time.

Differentiating (6) with $I(t') = at' + b$ $(a < 0)$, the maximum for $I_{\text{eff}}(t)$ is obtained for:

$$t_{\max} = \frac{b(n+1)\tau}{-a\tau + b} \quad \text{with} \quad \tau = RC$$

or, introducing the total drift time $t_{\text{D}} = -(b/a)$,

$$X_{\max} = \frac{t_{\max}}{\tau} = \frac{(n+1)t_{\text{D}}}{\tau + t_{\text{D}}}$$

$$X_{\max} = \frac{(n+1)t_{\text{D}}/\tau}{1 + t_{\text{D}}/\tau} \tag{7}$$

In practice one has $\tau \simeq 5 - 10$ ns and $t_{\text{D}} \simeq 500$ ns.
So

$$X_{\max} = \frac{t_{\max}}{\tau} \simeq n + 1 \tag{8}$$

This has to be compared with (5) in case of an impulse input. For $n = 3$ (practical value), one gets $X_{\max} = 2x_{\max}$, i.e. the maximum of I_{eff} is at $t_{\max} = 2t_{\delta}$.

3.2.3 experimental constraints

The time between two crossings in the LHC is foreseen around 15 ns. That means very fast readout electronics. A peaking time $t_{\delta} = 20$ ns is chosen for the time being. Following the previous estimates that means I_{eff} is maximum at $t_{\max} \simeq 40$ ns. These values have been used to design a track-and-hold integrator which picks up the $I_{\text{eff}}(t_{\max})$ value and integrates it for a fixed time ΔT. This yields a charge ΔQ which is recorded in an ADC. Therefore to reproduce the collected charges ΔQ, it is necessary to simulate the $I_{\text{eff}}(t_{\max})$ values of output currents corresponding to the drifting of charged hits (ΔT is a constant-free parameter).

Discussion:

As one can notice in (7), the value of $t_{\max}$ depends on the drift time t_{D} and on the value for n. In the case of a general $\vec{E}$ field, the drift time is no longer a constant as the drift velocity is not saturated in the experimental conditions (E around 1 kV/mm).

Nevertheless, for a given typical n value (3 or 4), and for a structure where $\vec{E}$ is not too variable (except in tiny regions as described in the following parts), one can fix a $t_{\max}$ value which is typically

$$t_{\max} \simeq 2t_{\delta}.$$

Then the current value $I_{\text{eff}}(t_{\max})$ is tracked.

3.3 Collection Simulation, Main Steps

In order to simulate the current response to a shower developed in the calorimeter, the hit banks produced by GEANT are used and *electric field maps* with a good accuracy (better than 1%) are produced.

3.3.1 define "single charges" from hit information

First of all it is assumed that energies deposited in LAr are uniformly distributed along corresponding track segments. So each segment of length L_i with a deposited energy E_i is divided into equal subsegments of length around ℓ_o. The real length ℓ_i of each subsegment is defined by

$$N_i = \left[\frac{L_i}{\ell_0}\right] + 1 \text{ and } \ell_i = \frac{L_i}{N_i}$$

where the square brackets denote the integer part. Each subsegment carries an energy $E_{ij} = E_i/N_i$ and a charge $Q_{ij} = E_{ij}/W_{\text{ion}}$ measured in unit of elementary charge. W_{ion} is the ionising energy in LAr to produce a pair Ar^+e^- ($W_{\text{ion}} = 23.6$ eV).

The choice for ℓ_0 is dictated by two opposite constraints: ℓ_0 has to be as small as possible to approximate a subsegment as a single charge, and large enough to minimize CPU time. Without loss of accuracy an ℓ_0 value of 200 μm is chosen.

3.3.2 electric field

For the various designed geometries electric field maps are produced in the folds of the accordion. The PRIAM package is used to solve a Poisson equation in two dimensions using a triangular mesh. It provides at each node the electric field components (E_x, E_y and $E_z = 0$). Up to now, those numerical values for field components are interpolated to produce a Cartesian mapping.

Several pitches of this mapping were tested and within a whole accuracy of 1%, a pitch equal to 100 μm was chosen.

3.3.3 drifting of each "single charge"

As explained in section 3.1, a negative charge Q_{ij} drifts in the opposite direction of the $\vec{E}$ field. The resulting current is

$$i(t) = \frac{Q_{ij}}{V_0}\vec{E}\cdot\vec{v}$$

The drift velocity is a function of the electric field and for $|\vec{E}|$ greater than 0.1 kV/mm, a linear approximation is adopted (region of interest is around 1 kV/mm):

$$v = a + b|\vec{E}|$$

with

$$\begin{aligned} a &= 2.3 \times 10^{-4} \text{ cm/ns} \\ b &= 0.17 \times 10^{-4} \text{ cm}^2\text{/ns/kV} \end{aligned}$$

3.3.4 charge recombination

After ionisation, the fraction of electrons which are really collected depends on both the number of Ar^+e^- pairs produced and the electric field value. In fact the number of free electrons produced by a minimum ionising particle (mip) saturates for E field values greater than 10 kV/cm [6].

A partial charge recombination is possible at lower E field. Two competing processes are gemellar recombination and columnar recombination.

- The initial (gemellar) recombination might occur at the very beginning of the drift process: a free electron just created is driven back to an ion and recombines with it. The Onsager formula [7] which expresses the fraction of e^- yield at low field, contains a characteristic length (thermalisation length) equal to 28 nm in LAr. Therefore, in the present simulation, this effect can be neglected after the first step in time for any drifting charge (Such a step corresponds to at least 9 or 10 μm).

- The columnar recombination is due to the large ion density produced by dE/dx along the initial track. In such a case, electrons drifting towards the cathode can be trapped by these ions.

These two processes are competing: at high field the gemellar recombination decreases, and with a high ion density the columnar recombination increases. What about these effects in the present design of the detector? The field value is chosen around 10 kV/cm in the constant regions. The initial ionising track and the main components of its shower are far from the perpendicular direction with respect to cathodes.

The charge recombination effect can therefore occur mainly at the very beginning of the drift process in regions of low E field values (gemellar effect in folds). Indeed in concave parts of folds the E field is only 30% of the nominal constant value E_0, and it increases by 10% above E_0 in the vicinity of convex parts. On top of that one has to take into account the folding of the initial current from electrodes with the bipolar response of the electronics. It is easy to check that those recombination effects could affect mainly the pair production in the vicinity of the leader folds (either concave for the A track or convex for the C track).

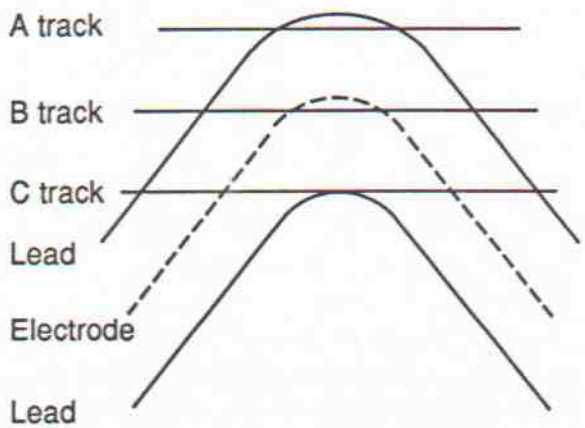

For purely geometric reasons, in a region of very low E field values along an ionising A track, the number of e^-Ar^+ pairs is only a small fraction of the corresponding number for a B track (in the electrode vicinity) or for a C track.

For a B track, in a region of low field below the electrode, a sizeable recombination effect could affect the collected current. But the net effect of the folding with the electronics bipolar response is a very poor contribution to the resulting signal anyway.

For a C track, the field in the vicinity of the fold is 10% higher than the nominal field ($E_0 = 10$ kV/cm) and the corresponding recombination is similar to the one for the nominal field E_0.

To check this recombination effect, experimental data from measurements in LAr were used in Monte Carlo simulations [8]. (In these data, charge combination effects – including columnar effect – on the current are about 20% for an electric field ratio of 0.25 and 1% for a field ratio of 1.1. The columnar effect is certainly very low in our case. Anyway these extreme effects were used to check the charge combination effect on the resulting recorded current.)

At the level of the present accuracy of these simulations, no significant effect on the resulting currents collected in the apparatus can be retained – except maybe a whole effect on the total collected current less than 0.5%.

3.3.5 numerical calculation of drift currents

Owing to the non-uniform electric field, numerical integration is used along the drift path in the folds. The elementary drift time is $dt = 2$ ns which corresponds roughly to a path $dl = 10$ μm which is largely compatible with the electric field map accuracy. In the vicinity of the electrode, the drift time is corrected according to the remaining distance dl_1:

$$dt_1 = \frac{dl_1}{dl} dt.$$

The elementary drift currents as given by (1) are then recorded.

3.3.6 output signal

The characteristic triangular shape distribution for the current $I(t)$ induced by the drifting charged segment results from a pile-up of partial currents produced by drifting elementary charges (see Fig. 3.1.1). As explained in section 3.2 this current $I(t)$ is then folded with the impulse response of the bipolar filter (see Fig. 3.1.2). The maximum of the resulting I_{eff} current is recorded at $t_{\mathrm{max}} = 2t_\delta$.

3.3.7 N-tuple from these simulations

Simulation results are stored in an N-tuple which contains for each primary, the total deposited energy in LAr and the corresponding total current recorded. The same quantities are available for each stack.

In order to reproduce the experimental cabling, an electronic cell is defined. For this, the apparatus is divided into two or three compartments along the incident particle direction. Each one of those parts is divided in a direction parallel to the folds (pitch of

2.5 cm) and cells are grouped by sets of three to form readout cells. The N-tuple contains recorded currents in each readout cell (for a given event a set of 7×7 readout cells in front of the incident particle is kept).

At this level of the simulation, data and Monte Carlo events are analysed in the same way.

3.3.8 current maps

Tracking each single charge (hit) in an inhomogeneous electric field means a huge amount of CPU time. So field maps are replaced by current maps which are used to perform interpolations.

Current maps are produced from electric field maps. Starting from each node of a given electric field map, a unit charge drifts and reaches the electrode. The corresponding induced current is folded with the impulse response of the electronics. A new map, current map is done with these current values at each node. With a real single charge Q_{ij} created at a given point, it is then easy to interpolate the current value after charge normalization. In this way all the currents are obtained without any new tracking.

In the case of electron showers and starting from hit banks as produced by GEANT, it takes about 2 s/GeV to produce currents with electric field maps and 0.12 s/GeV with current maps!

Current maps are therefore produced systematically from electric field maps for the various geometries which are designed.

4 Parallel Geometry (1990 Prototype)

4.1 Geometry

4.1.1 general considerations

The parallel geometry accordion calorimeter is simulated with accordion shaped absorbers and electrodes in a bath of LAr. Incident particles travel along the Z axis (see Fig. 1) and hit the calorimeter at $Z = 0$. Each absorber sheet is 2.2 mm thick and is composed of a 1.8 mm lead core cladded on each side with 0.1 mm of glue and 0.1 mm of stainless steel. The electrode sheets are 0.4 mm thick. They are assumed to be made up of a 0.07 mm copper core cladded with 0.165 mm of kapton on each side. Both the absorber and the electrode sheets, which are separated by a LAr gap of 1.9 mm, have an accordion fold length of 40.1 mm, 16 bend angles of 90° and a bend radius of curvature of 3 mm (measured from the center of curvature to the middle of the sheet thickness). A total of 48 absorber sheets each 37.5 mm wide in the Y direction were simulated. The actual materials used in the simulation are listed in table 1.

The readout cells are composed of 3 electrodes in X giving a granularity of 2.715 mm, and 2.5 mm strips in Y, yielding a total of 16×15 readout cells on the calorimeter face. The average thickness of the calorimeter for normal incidence is 25.4 X_o.

4.1.2 optimisation of the geometry

The parameters of the geometry were chosen [5] to optimise the uniformity of the LAr thickness traversed for normal incidence (see Fig. 2). This method has been quite successful in optimising the response uniformity for electrons.

This optimisation is performed using non interacting pseudoparticle (geantinos). To first approximation, neglecting charge collection effects, the response to electrons is proportional to the LAr traversed by the electron shower. Therefore local averages of the geometrical LAr length traversed are related to the response to electrons.

4.2 Field Maps

The electric field in the bending region is calculated using a finite elements method [9]. The domain on which the Poisson equation is solved is a triangular mesh. The triangle size is less than 100 μm in the bending region (see Fig. 3). A contour plot of the electric field strength for half a fold is shown on figure 4 : arrows give the direction of the field from one side to another side of the electrode, their lengths give the amplitude. The readout electrode separating the two LAr gaps is held at $V_o = 2$ kV while the absorber sheets are connected to ground. In the constant field region the field strength is 10.53 kV/cm for a gap of 0.19 cm. In the bending region, it ranges from 10 kV/cm in the region of convex bend to 3 kV/cm in the region of concave bend (see Fig. 5).

4.3 Results

4.3.1 general considerations

energy measured Unless otherwise mentionned, the charge collection and readout are not simulated on this chapter on the parallel geometry. The energy obtained from the Monte Carlo is therefore the energy loss by ionisation in the active LAr. Electromagnetic showers are simulated down to 10 keV for electrons and photons.

cryostat simulation The material in front of the active part of the calorimeter was simulated as to reproduce the experimental setup. Table 2 shows the types of "cryostat" considered. Unless otherwise written, the 1.184 X_0 type was included in the simulation. The mean and the rms of the energy loss in the simulated cryostat are shown in figure 6 for different electron energies.

electron data sample Table 3 shows the various Monte Carlo data samples simulated. E_{cut} corresponds to the cutoff energy for the electrons and photons below which the showers simulation is stopped (unless otherwise mentioned, the results presented in this chapter are for $E_{\text{cut}} = 10$ keV). The angles θ and ϕ fix the incidence of the electrons on the calorimeter face. Events are simulated with impact point uniformly distributed over a readout cell. Not all these data samples have yet been analysed, and work is continuing.

timing The results presented in this chapter were obtained using GEANT version 3.1416 with correction cradle version 3.1407. The simulation took 16.0 s/GeV/cpu on a 4cpu DN10000 Apollo computer for a 10 keV cut on the electrons and photons. This goes down to 9.33 s/GeV/cpu (5.22 s/GeV/cpu) for a 100 keV (1 MeV) cut.

4.3.2 electron energy response

leakage In the simulation, the energy escaping the calorimeter was collected to measure the energy leakage. Figure 7 shows the mean and rms of the leakage energy for electron showers of various energies and with various cryostats used. It is about 1% for 200 GeV electron showers, to be compared with the experimental value of $< 0.3\%$ [3].

uniformity The Monte Carlo results on the uniformity of the response to electrons has already been reported [2, 3]. Figure 8 shows the X and Y uniformity of response for 90 GeV electrons expressed in percent of deviation from the average. The broad maximum of the response in X corresponds to the broad maximum of LAr length traversed in figure 2, which corresponds to the lack of everlap of the electrode corners. Both the response in X and Y show a global decrease of about 1% near 0.5, the edge of the readout cell. This is an effect of the 3x3 cell clustering and disappears when 5x5 cell clusters are used.

Fig. 9 again shows the variation of energy measured as a function of impact point along the X direction, both for real data and simulation; on the left figure charge collection simulation is included, which is not the case for the figure on the right. this time including charge collection simulation. The energy is calculated in a 3x3 cell cluster. A good agreement is obtained when charge collection with shaping is taken into account,

mainly in the center of the cell where the bump is well reproduced. It is clear that a full simulation including charge collection and convolution with electronics is necessary to fully reproduced data.

The X and Y uniformity of response have been fitted with a 5 parameter even Fourier serie and a 2 parameter parabola respectively. These parametrisations can then be used to correct the response on an event-by-event basis. Figure 10 shows the rms of the uniformity of response in X for various electron energies before and after a XY energy independent correction. The XY correction do not alter the mean of the energy distribution.

energy spectrum The energy reconstructed for 90 GeV incident electrons not corrected for XY variation is shown on Fig. 11; the agreement is good between data and simulation.

The XY correction reduces the width of the energy distribution and improves its gaussian shape, but does not change its mean. Figure 12 shows an example of an energy spectrum after XY correction.

sampling fraction The amount of energy deposited in the LAr by an electron shower depends on the size of the cluster used to measure it as well as on the material in front of the calorimeter. Figure 13 shows the sampling fraction, defined as the ratio of the measured energy over the electron energy, for 30 GeV electrons for various cluster sizes and cryostat thicknesses. A value of 14.68% is found for a 3x3 cluster with a 1.184 X_o thick cryostat in front.

linearity The sampling fraction is found to vary by less than $\pm 0.2\%$ for electrons between 30 and 200 GeV (see Fig. 14).

shower size Information on the longitudinal and lateral shower size can be obtained by comparing the amount of energy deposited in various stacks (longitudinally) and in various cells (laterally).

Although the simulation allows the study of the amount of energy in each of the 16 stacks in depth, only the 8:8 (2-compartment) and 5:5:6 (3-compartment) groupings exist experimentally. Table 4 compares three shower width variables with data [3] for three types of cryostat simulated and two electron energies.

The first width variable is the ratio of the energy contained in the first 8 stacks of the calorimeter (2-compartment case) over the total energy, for 3x3 cell clusters. Disagreement with data is not understood, and cannot be explained easily by allowing more simulated material in front of the calorimeter.

The other width variables studied are the fraction of 3x3 cell cluster energy in the first compartment (stacks 1 to 5) and the middle compartment (stacks 6 to 10) for the 3-compartment case. Here we have a good agreement with data for a simulated cryostat of 1.184 X_o.

Laterally the simulation gives a ratio of the 3x3 and 5x5 cluster energy of $(93.98 \pm 0.02)\%$ and $(94.00 \pm 0.02)\%$ for 30 GeV and 200 GeV electron showers respectively.

4.3.3 electron energy resolution

The energy resolution for electrons is obtained from the ratio of the mean and the standard deviation of the electron response, both obtained by fitting a gaussian to the energy spectrum. Figures 15 and 16 show the resolution obtained for 30 GeV electrons without and with XY correction respectively, for various cryostat thicknesses and cluster sizes. The resolution is seen to be improved by the XY correction, while it deteriorates with increasing cryostat thickness. The difference in resolution between 3x3 and bigger cell clusters is also evident, which is not the case for the testbeam data [3]. The uncorrected energy resolution obtained for 5x5 cell clusters for 30 GeV electron showers is found to be (1.56±0.02)%, (1.60±0.09)% and (1.84±)% for electrons and photons simulation down to 10 keV, 100 keV and 1 MeV respectively.

Figure 17 shows the energy resolution for electrons of energy between 30 and 200 GeV with 1.184 X_o cryostat and 3x3 cell cluster. A XY energy independent correction was applied. The energy dependence is fitted to

$$\frac{\sigma}{E} = \frac{a}{\sqrt{E}} \oplus b$$

where the sampling term $(a/\sqrt{E})$ and the constant term (b) are added in quadrature. No noise term was included since electronic noise was not simulated. The fit yields $a = (8.61 \pm 0.15)\%$ GeV$^{1/2}$ and $b = (0.234 \pm 0.075)\%$. The conditions used to obtain this result are believed to be similar to the experimental conditions leading to the result quoted in [3]. The simulated resolution is approximately 10% better than the experimental one. Values of a and b obtained for other simulated conditions are listed in table 5

The energy resolution as a function of the θ angle of incidence (for ϕ=0, see Fig. 1) was also studied. Figure 18 shows the resolution for 90 GeV electrons for θ between -20 and 80 mrad for 3x3 and 5x5 cell clusters. We notice that the resolution improves slightly for $\theta > 0$ before worsening considerably for $\theta > 60$ mrad.

The XY dependence of the response decreases away from θ, which could account for the improved uncorrected resolution. With increasing θ angle, the change in sampling fraction and frequency worsens the resolution. An optimum resolution may exist for an angle between 20 and 50 mrad, if XY correction is not used. It is worth noting that the XY corection depends on θ, which could make XY correction difficult for non normal incidence electrons.

4.3.4 electron position reconstruction

The electron shower position can be obtained by computing the first moment of the energy distribution in a cluster. This can then be compared, on an event by event basis, with the electron impact point in order to obtain the mean offset and the resolution of the position reconstruction.

Along X, the correlation between the reconstructed shower position and the electron impact point is found to be practically linear (see Fig. 19). The width of their difference gives the position resolution in X. The reconstructed shower position is biased near cell edges due to the fact that odd number of cells are used in clustering in X (and Y). This

effect, stronger for small clusters, produces a slope of 0.938±0.002 for 3x3 clusters (as shown on Fig. 19) and 0.986±0.003 for 7x7 clusters.

Along Y, the reconstructed shower position must be corrected as indicated in [2, 3] before comparing it with the electron impact point. Figure 19 shows the uncorrected correlation between the reconstructed Y position and the electron Y impact for 90 GeV electrons. The clustering effect at cell edges is also visible.

For normal incidence 90 GeV electrons and using only the first of two samplings in depth (that is using only 8 stacks), the simulation gives

$$\sigma_X = (0.45 \pm 0.01) \text{ mm}$$

$$\sigma_Y = (0.37 \pm 0.01) \text{ mm}$$

to be compared with the experimental results [3] (0.394 ± 0.002) mm and (0.505 ± 0.001) mm respectively. The difference between data and Monte Carlo (in particular the fact that $\sigma_X < \sigma_Y$ is not reproduced) is not yet understood.

While the number of stacks used for clustering is limited to the electrode fabrication for the experimental data, any number of stacks (up to 16) can be used in the simulation. Figures 20 and 21 show the X and Y position resolution respectively, for 90 GeV normal incidence electrons using a variable number of stacks in depth for clustering. While the Y position resolution is found to improve with increasing number of stacks used in depth with small dependence on the cluster size used, the X resolution reaches its minimum for about 6 stacks in the case of 3x3 clustering, corresponding to the location where about half the shower energy is deposited. This behaviour disappears if the cluster dimension in Y is reduced or if the cluster dimension in X is increased. In both cases, the X resolution does not deteriorate much when more then half the shower energy is included.

These results suggest that a 3x1 cluster might be favorable to measure the X position of a 90 GeV electron shower if more than 6 stacks are used for the position reconstruction.

Also of interest is the offset or bias in the reconstruction of the shower. No bias is found in Y as expected. Figure 22 shows the offset in the reconstruction of the X position of 90 and 200 GeV electron showers as a function of the number of stacks used in depth. The effect of the accordion structure is evident. It is important to note that in this case the predicted effect is still of the order of the resolution if up to 8 stacks are used. The offset is found to be independent of the cluster size, but varies slightly with energy as the shower profile changes.

The knowledge of such a systematic offset in the reconstruction of the X position of electron showers is of course crucial when matching the calorimeter result to other (inner) detectors in ATLAS. It might be better to stop the first compartment near an edge of the kapton sheet, which corresponds to half stacks in figure 22.

X OFFSET ≡ X calo − X particle

material	simulated material	density (g/cm^3)	rad length (cm)
lead	lead	11.35	0.56
copper	copper	8.96	1.43
stainless steel	iron	7.87	1.76
aluminium	aluminium	2.70	8.90
liquid argon	liquid argon	1.40	13.9
glue	plexiglass ($C_5H_8O_2$)	1.18	34.1
kapton	plexiglass ($C_5H_8O_2$)	1.18	34.1

Table 1: Simulated materials

material	thickness (cm)			
aluminium	2.0	2.0	2.0	2.0
vacuum	2.7	2.7	2.7	2.7
iron	0.3	0.3	0.3	0.3
liquid argon	1.0	1.0	1.0	1.0
air	15.0	15.0	15.0	15.0
liquid argon	5.0	10.0	15.0	20.0
total	26.0=0.826$X_\circ$	31.0=1.184$X_\circ$	36.0=1.543$X_\circ$	41.0=1.901$X_\circ$

Table 2: Four different types of cryostat considered. The material layers appear in the order they are simulated.

energy (GeV)	cryostat ($X_\circ$)	$E_{\rm cut}$ (keV)	θ (mrad)	ϕ (deg)	events
30	0.826	10	0	0	500
30	1.184	10	0	0	1300
30	1.543	10	0	0	1300
30	1.901	10	0	0	650
30	1.184	100	0	0	1300
30	1.184	1000	0	0	1600
90	0.826	10	0	0	400
90	1.184	10	0	0	700
90	1.543	10	0	0	700
90	1.184	100	0	0	100
90	1.184	10	-20	0	500
90	1.184	10	-10	0	500
90	1.184	10	10	0	500
90	1.184	10	20	0	500
90	1.184	10	30	0	500
90	1.184	10	40	0	500
90	1.184	10	50	0	500
90	1.184	10	60	0	500
90	1.184	10	70	0	500
90	1.184	10	80	0	500
90	1.184	10	100	0	500
90	1.184	10	150	0	500
90	1.184	10	200	0	500
90	1.184	10	250	0	500
90	1.184	10	300	0	500
90	1.184	10	350	0	500
90	1.184	10	50	90	500
90	1.184	10	100	90	500
90	1.184	10	150	90	500
90	1.184	10	200	90	500
90	1.184	10	250	90	500
90	1.184	10	300	90	500
90	1.184	10	350	90	500
150	0.826	10	0	0	400
150	1.184	10	0	0	400
150	1.543	10	0	0	400
200	0.826	10	0	0	100
200	1.184	10	0	0	300
200	1.543	10	0	0	300

Table 3: GEANT Monte Carlo samples simulated. See text.

energy (GeV)	cryostat ($X_\circ$)	2-comp $\frac{E(\text{front})}{E}$ (%)	3-comp $\frac{E(\text{front})}{E}$ (%)	3-comp $\frac{E(\text{middle})}{E}$ (%)
30	0.826	88.7±0.3	57.1±0.4	39.1±0.4
	1.184	89.6±0.2	59.8±0.3	36.7±0.2
	1.543	90.7±0.1	63.2±0.3	33.7±0.2
	data	94.	59.	37.
200	0.826	78.8±0.7	39.6±0.8	52.0±0.5
	1.184	80.6±0.4	42.6±0.5	50.0±0.3
	1.543	82.4±0.4	45.9±0.5	47.5±0.3
	data	83.	45.	49.

Table 4: Comparison of simulated shower width variables with data. See text.

	3x3	5x5	7x7
0.826 $X_\circ$	$8.89 \pm 0.21\%$	$8.17 \pm 0.41\%$	$7.92 \pm 0.44\%$
	$0.00 \pm 0.24\%$	$0.413 \pm 0.081\%$	$0.524 \pm 0.067\%$
1.184 $X_\circ$	$8.61 \pm 0.15\%$	$7.75 \pm 0.16\%$	$7.86 \pm 0.28\%$
	$0.234 \pm 0.075\%$	$0.467 \pm 0.041\%$	$0.512 \pm 0.045\%$
1.543 $X_\circ$	$9.16 \pm 0.18\%$	$8.72 \pm 0.27\%$	$8.61 \pm 0.27\%$
	$0.00 \pm 0.39\%$	$0.421 \pm 0.057\%$	$0.413 \pm 0.057\%$

Table 5: Sampling (in $\text{GeV}^{1/2}$) and constant terms obtained for various cluster sizes and cryostat thicknesses. Energy independent XY corrections were applied.

Figure 1: View of the calorimeter in the $X - Z$ plane. The Z axis runs from left to right with $Z = 0$ at the face. The X axis runs upward. The horizontal line represents a noninteracting particle incident at $X = 0$ in the fourth readout cell in X. Polar coordinates are defined as usual: ϕ is the angle in the XY plane measured clockwise from the X axis and θ is the angle to the positive Z axis.

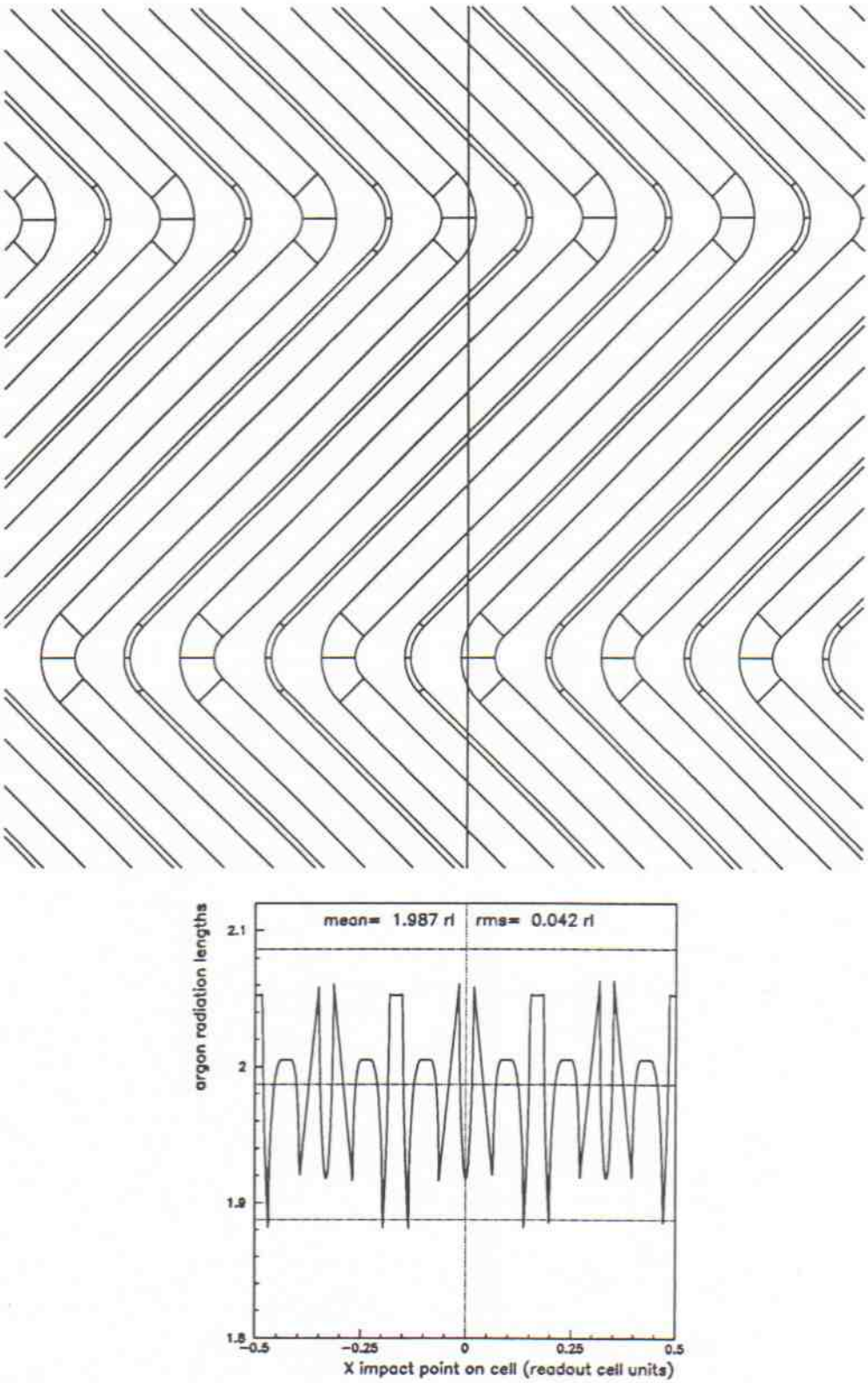

Figure 2: The bottom figure shows the LAr thickness traversed, in radiation length, as a function of X in cell units. The dotted lines show a $\pm 5\%$ band. From the top figure we see that $X = 0$ corresponds to the overlap of the absorber corners. The electrodes are also shown. Both figures have the same X scale.

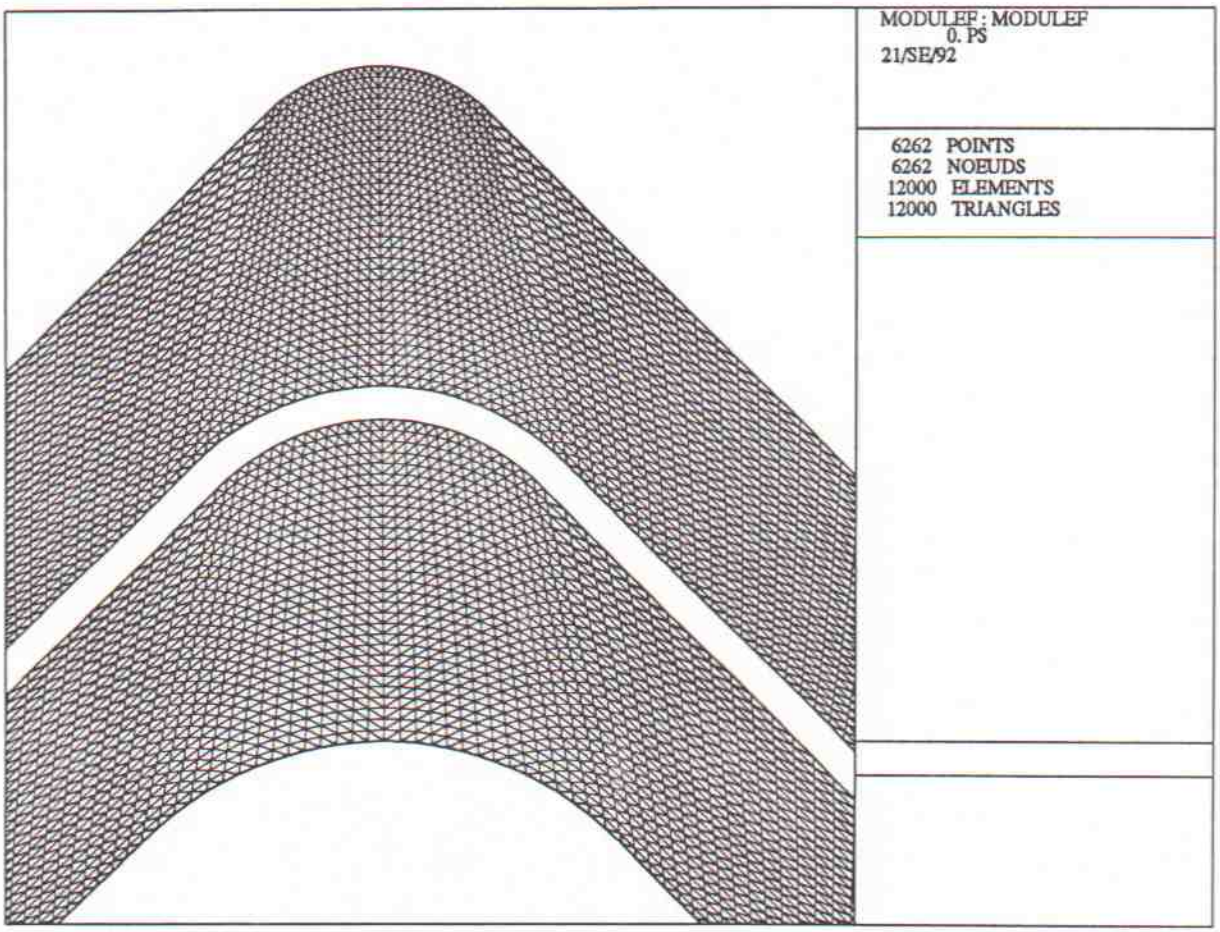

Figure 3: Mesh used for electric field calculation.

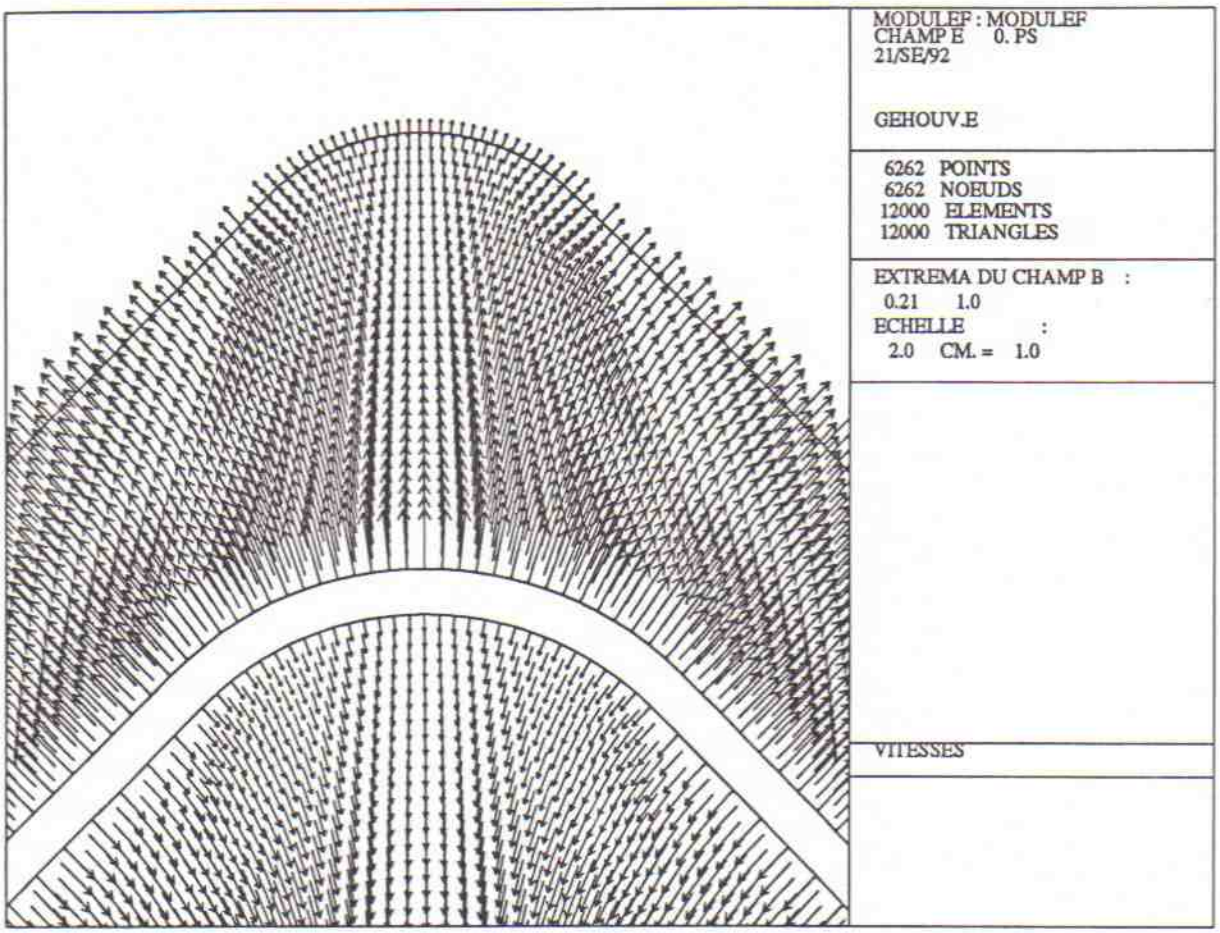

Figure 4: Electric field in a bend from one side to the other side of the electrode. Arrows represent the vector electric field; their length is proportional to the electric field strength.

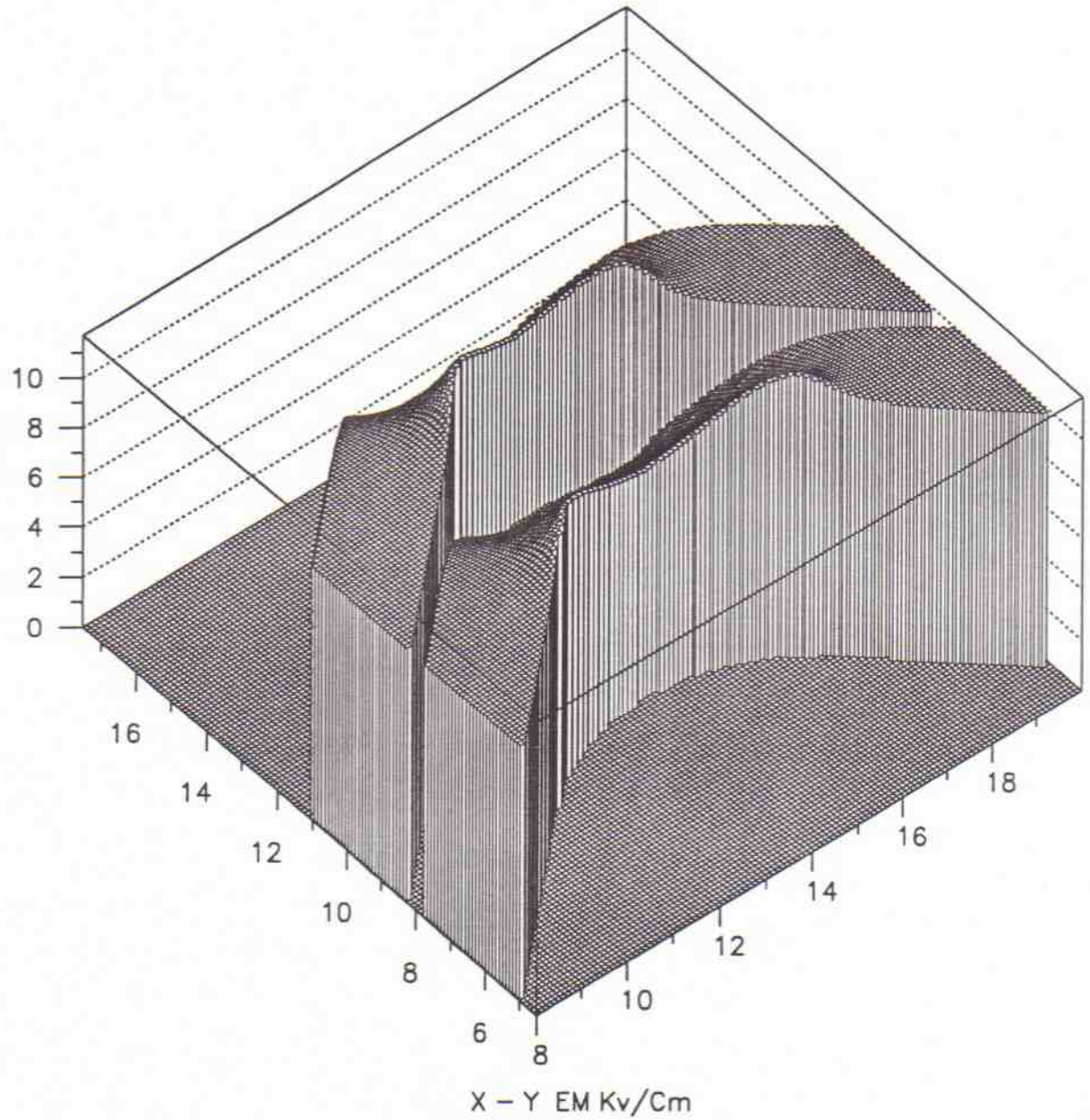

Figure 5: Electric field in kV/cm in a bend. It is maximum in the convex part, minimum in the concave one and constant in the parallel plate region.

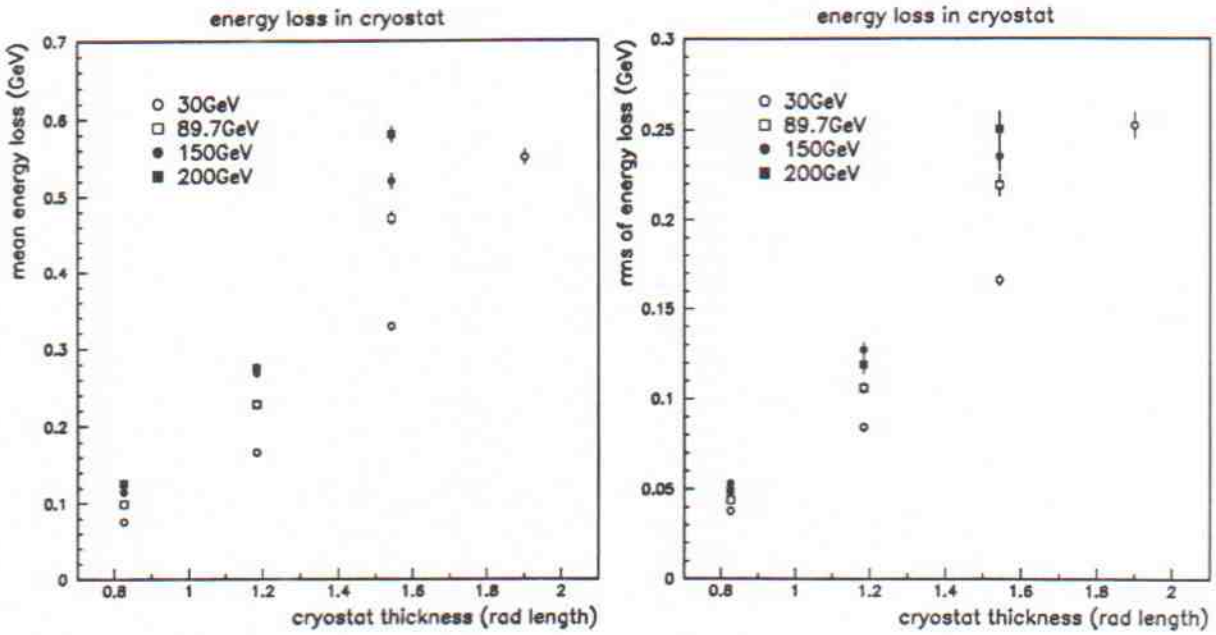

Figure 6: Mean and rms energy loss in the different cryostat considered for four different electron energies.

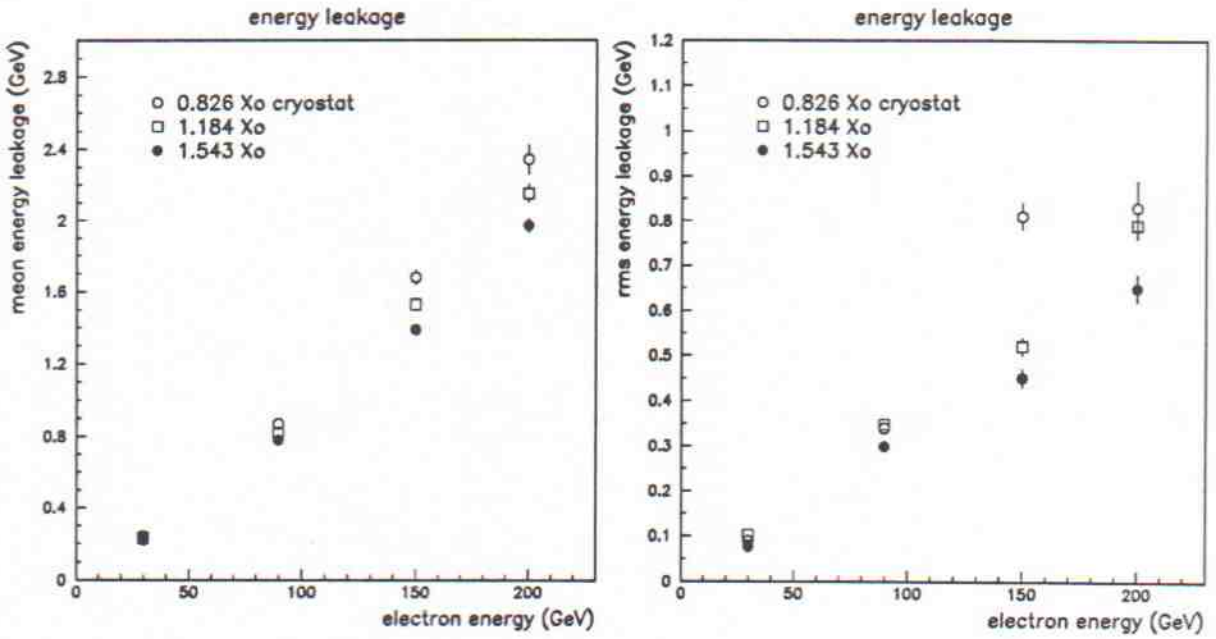

Figure 7: Mean and rms leakage energy for four different electron energies and various cryostats used.

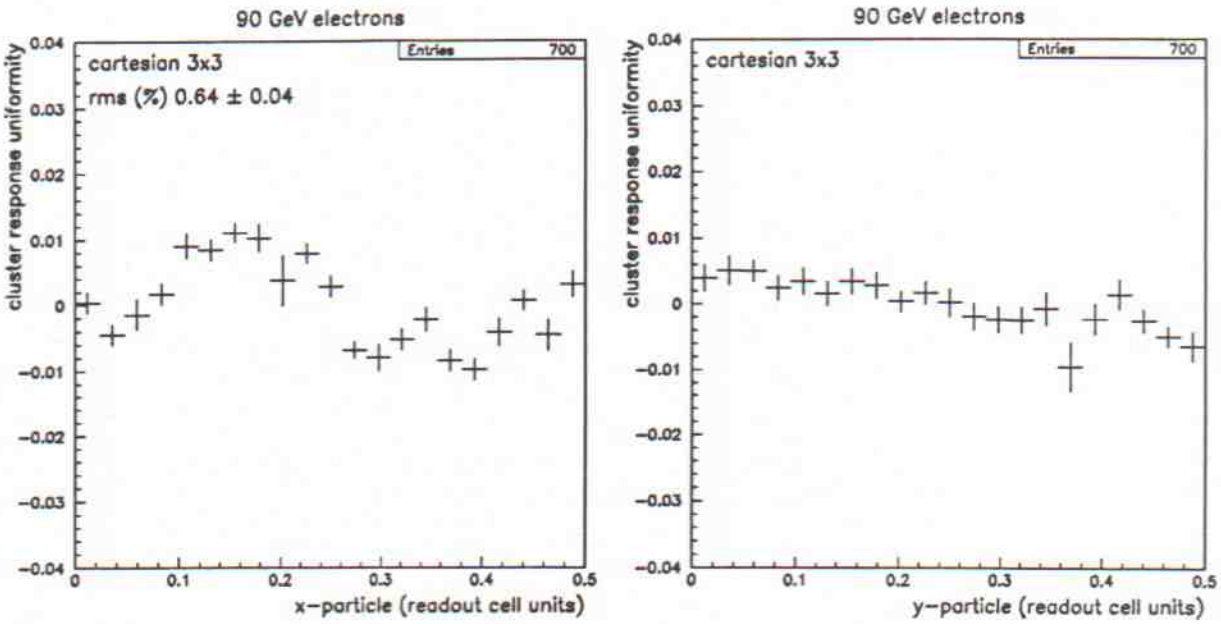

Figure 8: Uniformity of response in X and Y for 90 GeV electrons expressed in percent of deviation from average. 3x3 cluters used.

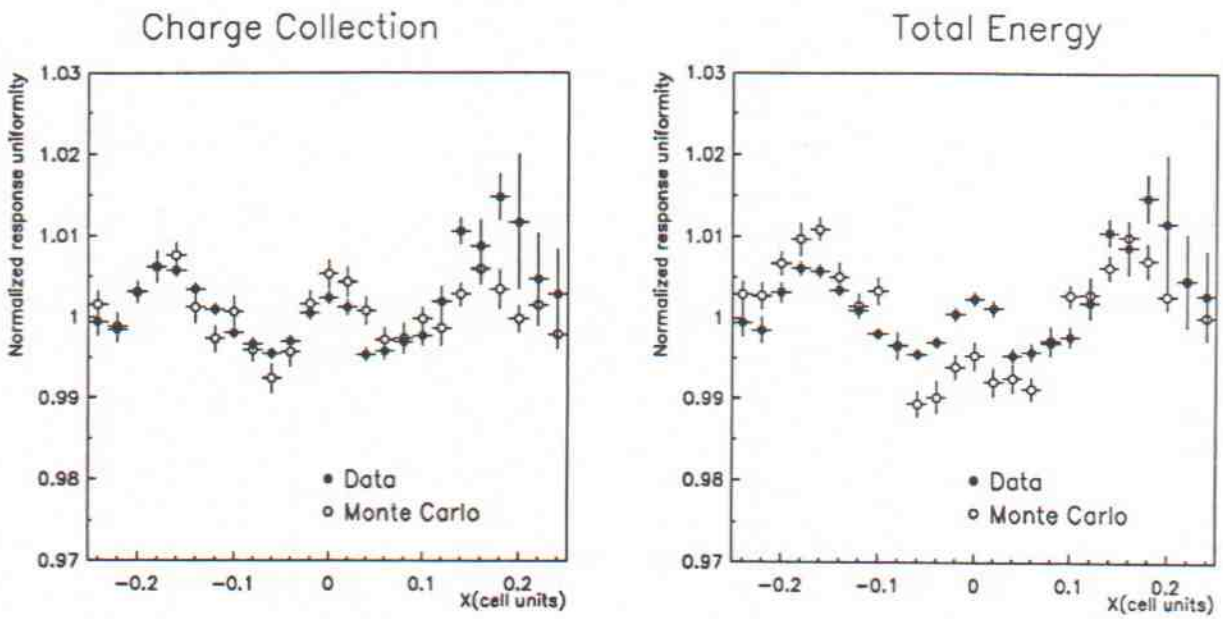

Figure 9: Uniformity of response in X for 90 GeV electrons for testbeam data and simulation. Charge collection has been simulated in the figure on the left, but not in the figure on the right.

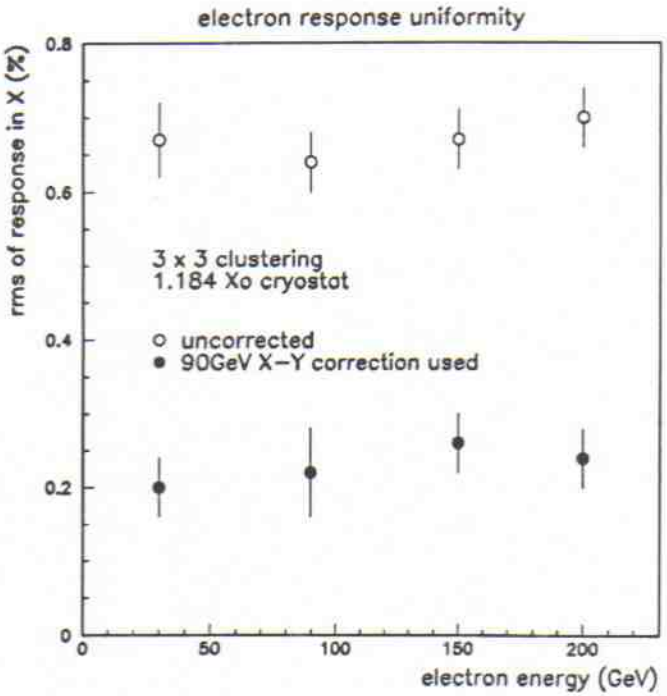

Figure 10: Rms of response in X for various electron energies before and after a XY energy independent correction.

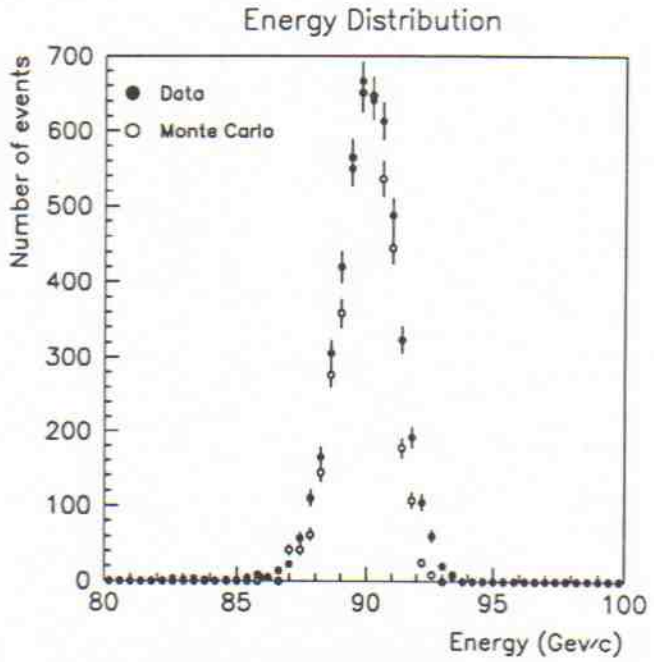

Figure 11: Energy distribution for 90 GeV electrons without XY correction.

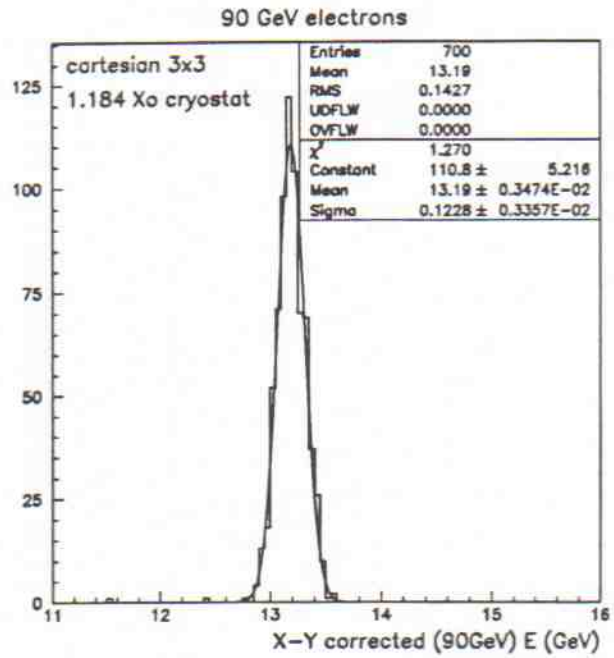

Figure 12: Energy distribution for 90 GeV electrons after XY correction. A cryostat $1.184X_o$ thick has been simulated and 3x3 cell clusters were used. The abscissa shows the energy deposited in the LAr.

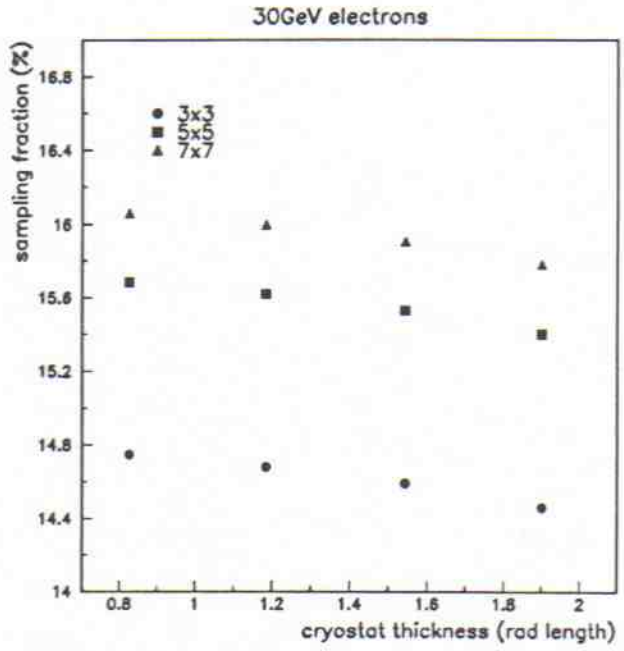

Figure 13: Sampling fraction measured for 30 GeV electrons for various cluster sizes and cryostat thicknesses. A cryostat $1.184X_o$ thick has been simulated.

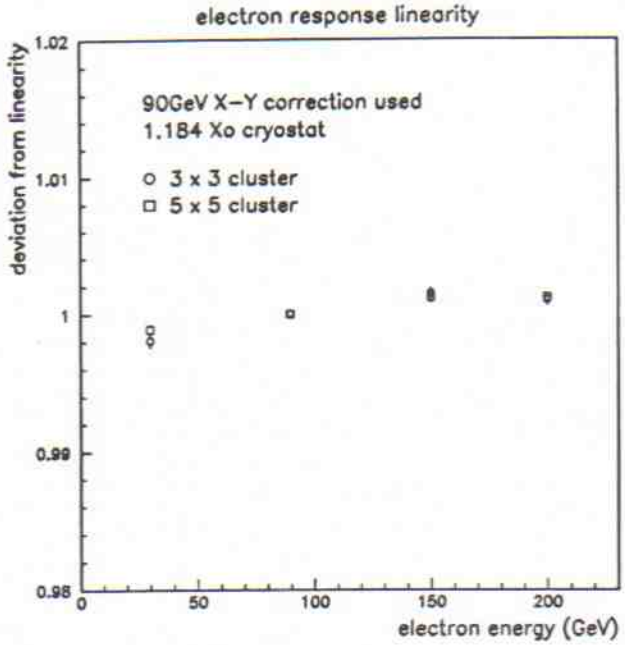

Figure 14: The deviation from linearity for electrons between 30 and 200 GeV normalised to 1 at 90 GeV.

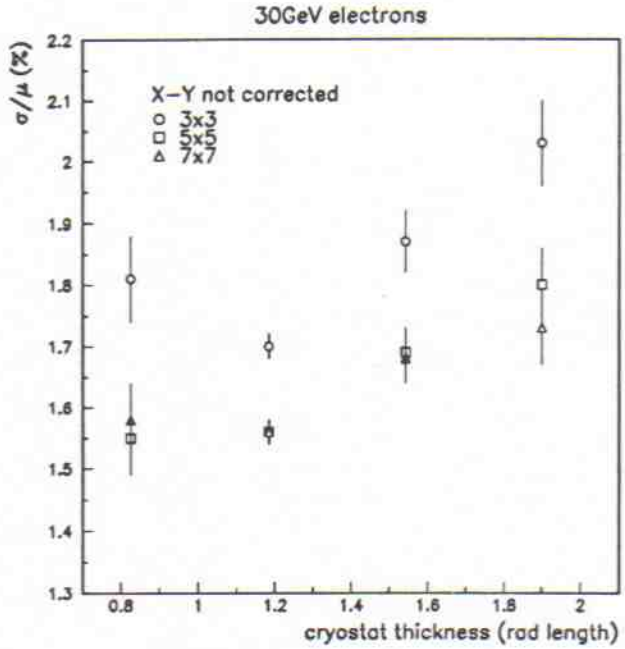

Figure 15: Energy resolution for 30 GeV electrons without XY corrections, for various cryostat thicknesses and cluster sizes.

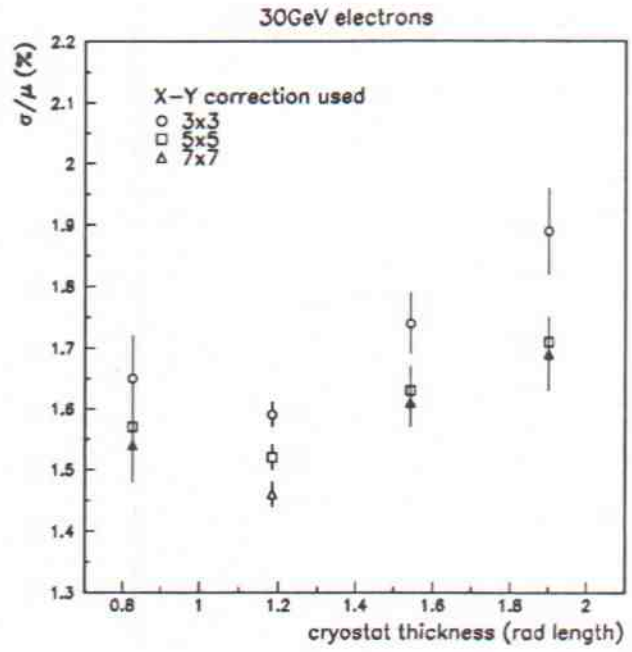

Figure 16: Energy resolution for 30 GeV electrons with XY corrections, for various cryostat thicknesses and cluster sizes.

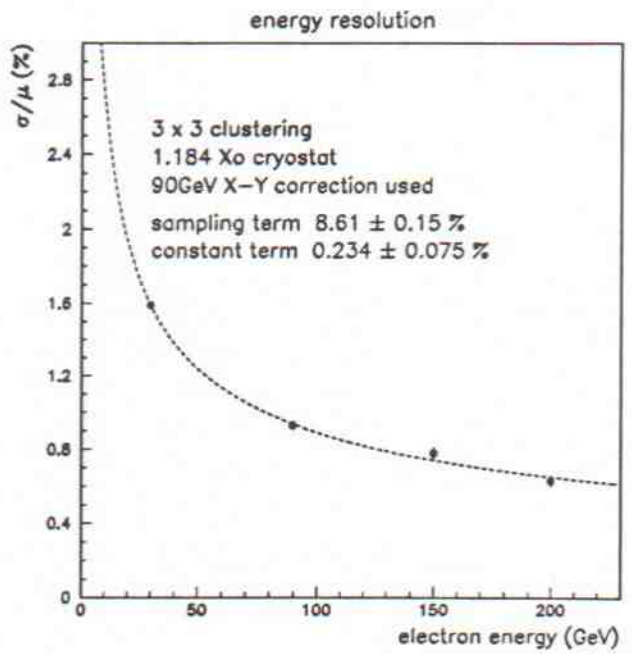

Figure 17: Energy resolution for electrons between 30 and 200 GeV. An XY energy independent correction was used.

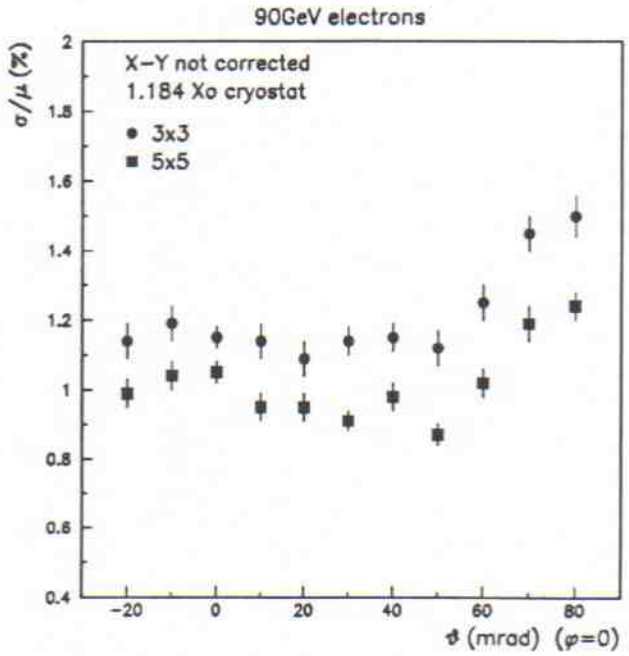

Figure 18: Energy resolution for 90 GeV electrons as a function of the angle θ (for $\phi = 0$).

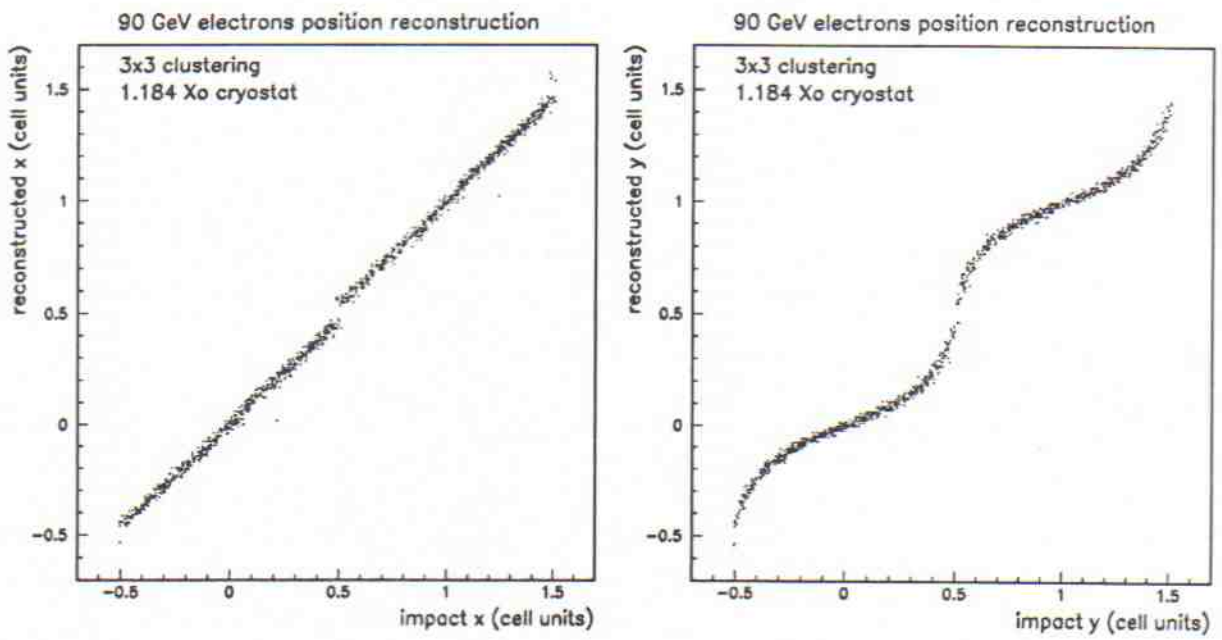

Figure 19: Reconstructed X and Y positions as a function of impact position (over two cells centered at 0 and 1) for 90 GeV electrons. One cell unit corresponds to 2.715 cm in X and 2.5 cm in Y. Note the clustering effect near cell edges.

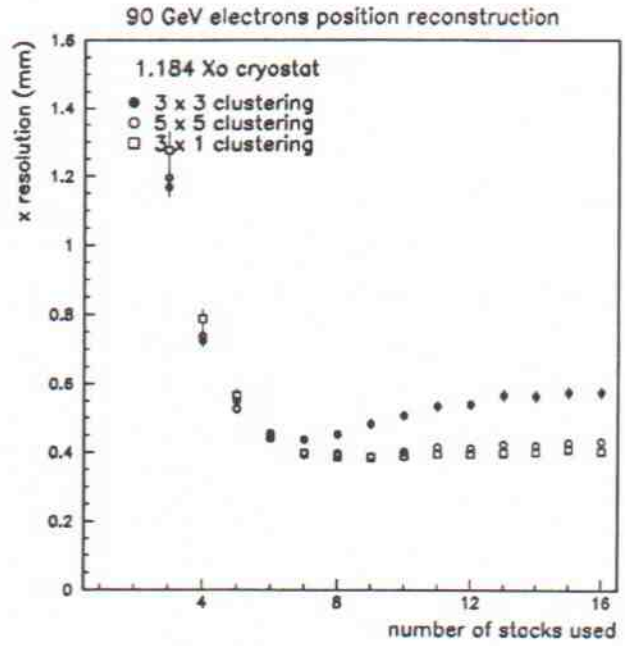

Figure 20: Position reconstruction resolution in X for normal incidence 90 GeV electrons as a function of the number of leading stacks (depth segmentations) used. Various cluster sizes were used.

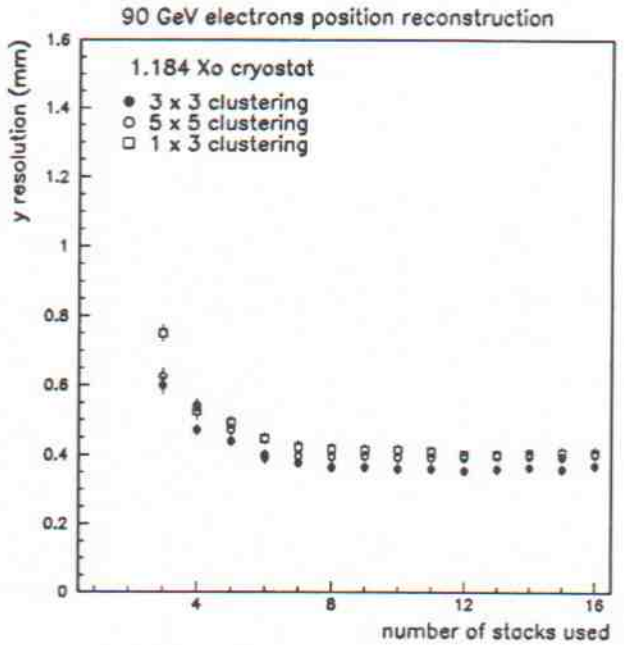

Figure 21: Position reconstruction resolution in Y for normal incidence 90 GeV electrons as a function of the number of leading stacks (depth segmentations) used. Various cluster sizes were used.

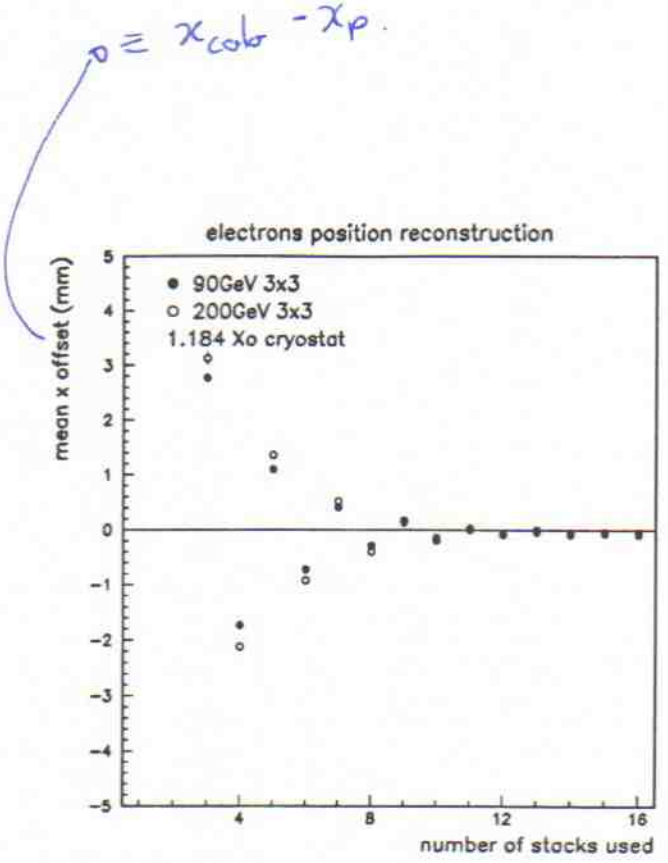

Figure 22: Offset or bias in the reconstruction of the X position for normal incidence 90 and 200 GeV electrons as a function of the number of leading stacks (depth segmentations) used.

5 Cylindrical Geometries (1991 Prototype)

5.1 Geometry

The two different geometries are described in details in [4] The first one, called projective geometry, is the simplest projective geometry we can conceive. Absorber plates are displayed all around the beam line with the folds parallel to it. The chosen angle, 0.341°, corresponds to a value of 1.9 mm of LAr gap at 20 cm from the entrance face of the calorimeter. This corresponds roughly to the maximum of the shower. The thickness of the LAr gap increases along the depth of the device (see Fig. 23). As a consequence, the electric field in the gap decreases. Therefore the energy collected will decrease with depth for a given time of collection.

It is possible to keep the LAr gap constant by adding an increasing thickness of a low Z material glued on absorber plates. This geometry with compensated gap is called compensated geometry (see Fig. 24). For the simulation results presented in this chapter on cylindrical geometries, the absorber plates is approximated by a 2.2 mm thick material, composed of an homogeneous mixture of 1.8 mm lead, 0.2 mm steel and 0.2 mm prepreg. It has been checked, in the case of parallel geometry, that results are equivalent with or without full cladding. The advantage of this approximation is a gain in computing time. Nevertheless, the simulation takes into account the cladding of the 2.2 mm thick absorber with prepreg layer of increasing thickness, in the case of the compensated geometry.

5.2 Field Maps

In the case of opening geometry, the LAr gap is increasing with depth. Since the voltage applied on the electrode is constant, the electric field strength decreases with depth in the calorimeter. Outside bends the LAr gap varies from 1.47 mm to 2.36 mm. The electric field is computed in each bends and a mean value is given in each sligthly opening straigth sections. Figure 25 shows the variation of the field strength in the middle of a bend, respectively at the inner, middle and outer radius of the calorimeter. The variation of the maximum value of the field in these three different positions is about 30%. The computation of the field strength in the compensated geometry is equivalent to the computation in a parallel geometry since the gap remains constant. It is 1.43 mm thick, compared to 1.9 mm in the parallel geometry, giving a field around 30% bigger (for the same applied tension).

5.3 Timing

Hits, as defined in chapter 3, are recorded onto cartridge for further charge collection simulation. A 90 GeV shower represents 4.5 Mbytes of information and requires 500 s processing time on HP730.

5.4 Results

Simulation is performed by sending electrons of fixed energy at normal incidence to the calorimeter face to cover a full readout cell which corresponds to three electrodes (3 ×

0.341°). Unless otherwise mentioned, charge collection simulation is performed for the results presented in this chapter on cylindrical geometries. The final energy is given by the energy contained in a 3x3 cell cluster as for testbeam data. The ratio of the energy measured in 3x3 cell clusters over the energy measured in 5x5 cell clusters is approximately 95%; simulation is in good agreement with this experimental result. As the impact point of an electron varies, there is a variation of absorber and LAr traversed by the shower and thus a variation of energy response. It is expected that this variation is bigger for the cylindrical geometry than for the parallel one because the gap is opening. This is also true for the compensated geometry. Figures 26 and 27 show this variation both for opening and compensated geometries. The periodicity is very well reproduced by the simulation. The amplitude is approximately $\pm 2\%$ and is better simulated in the compensated geometry than in the opening geometry. It is possible that the prototype calorimeter was slightly tilted during the data taking. This can explain the relatively smaller modulation.

To compare simulation with testbeam data for the case of the dependance of the energy as a function of the shower depth, it is assumed that the total amount of material in front of the calorimeter is 1.18 X_o as it has been measured for parallel geometry. The opening geometry is sampled in three sections in depth while the compensated one is sampled in two sections only. The total charge measured in the opening gap calorimeter shows some dependance on the depth at which the shower develops. This depth is parametrized by the fraction of the energy deposited in the front or the back section of the three compartments. Figures 28 and 29 show the total energy normalized to its mean value for 90 GeV electrons as a function of these two fractions. The agreement with data is relatively good except when the shower is developed very early. Either GEANT has some problem to reproduce ends of shower or the amount of front material is badly estimated. By comparison, curves with black stars represent the signal when the total ionisation signal is taken without electronics convolution. This illustrates very well the effect of opening gap. In the compensated geometry the variation of the collected energy as a function of the depth is smaller as it is shown on figure 30. The agreement with simulation is fairly good. In this case the total charge is not shown, since the time distribution of the ionisation does not depend on the depth.

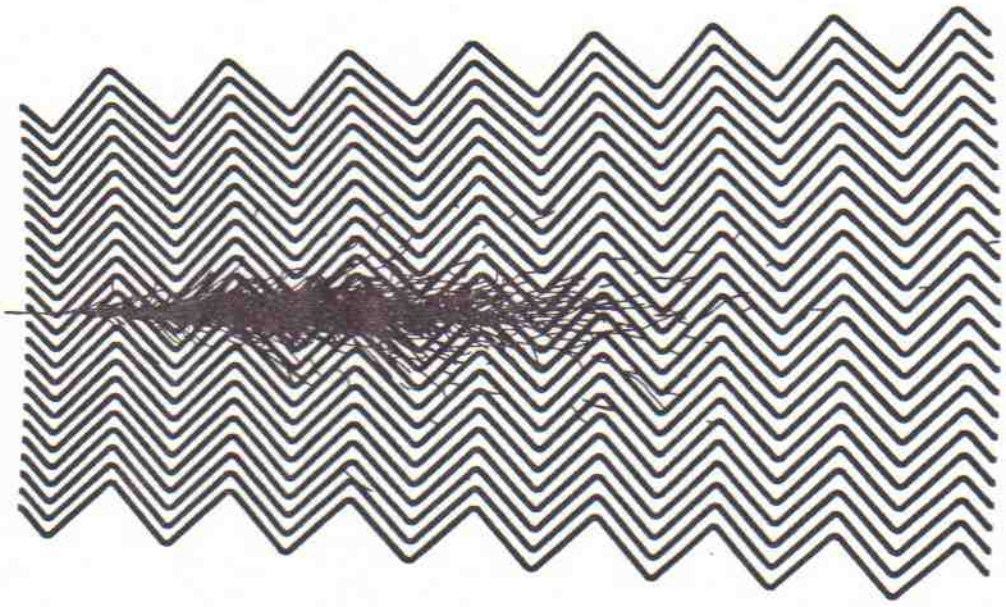

Figure 23: Section of the simulated projective geometry. Note that the accordion angles are constant and that the LAr gap increases with depth. A 100 GeV electron shower is also simulated. Only absorber sheets and charged tracks down to 10 MeV are shown.

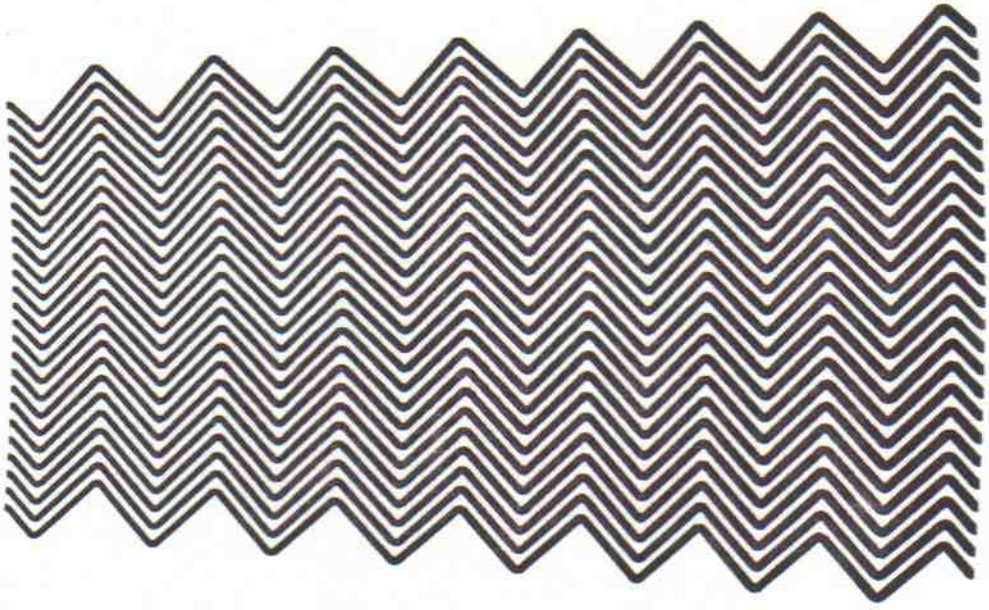

Figure 24: Section of the simulated compensated geometry. Note that the accordion angles are constant but that the absorber thickness increase with depth, keeping the LAr gap constant.

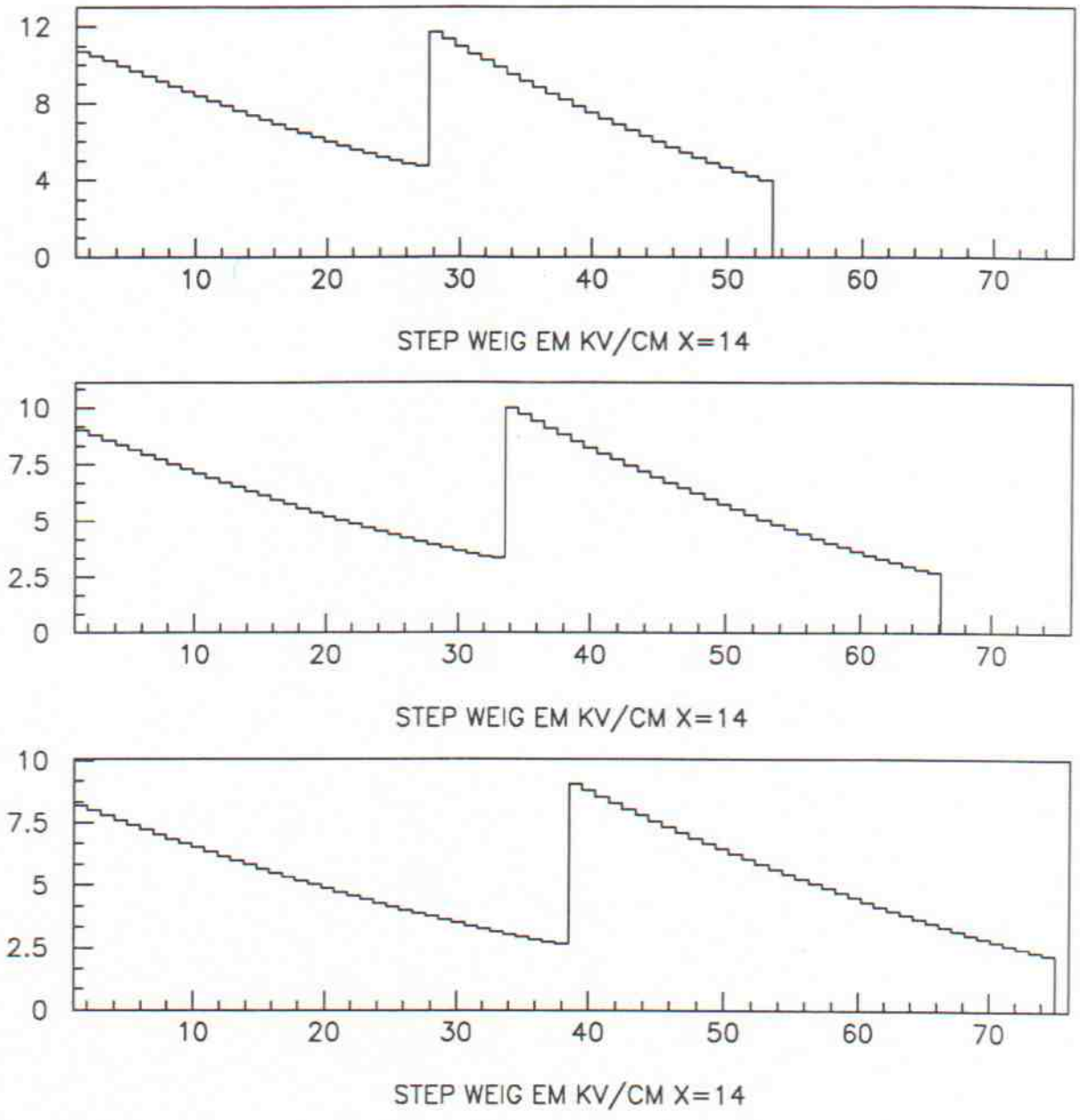

Figure 25: Variation of the electric field strength, in 100 μm steps, in the middle of a bend for 3 different depth positions in the calorimeter (front, middle and back for the top, middle and bottom figure respectively).

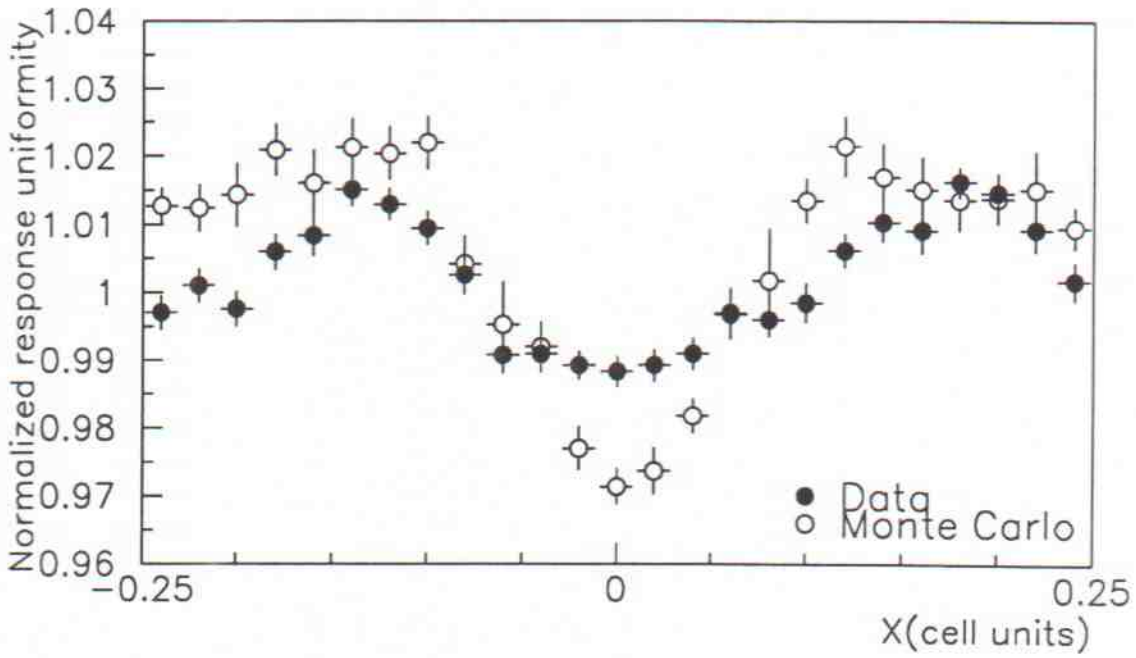

Figure 26: Variation of the energy response of the calorimeter normalized to the beam energy for 90 GeV electrons as a function of the impact point in the X direction (in readout cell units) for the opening geometry.

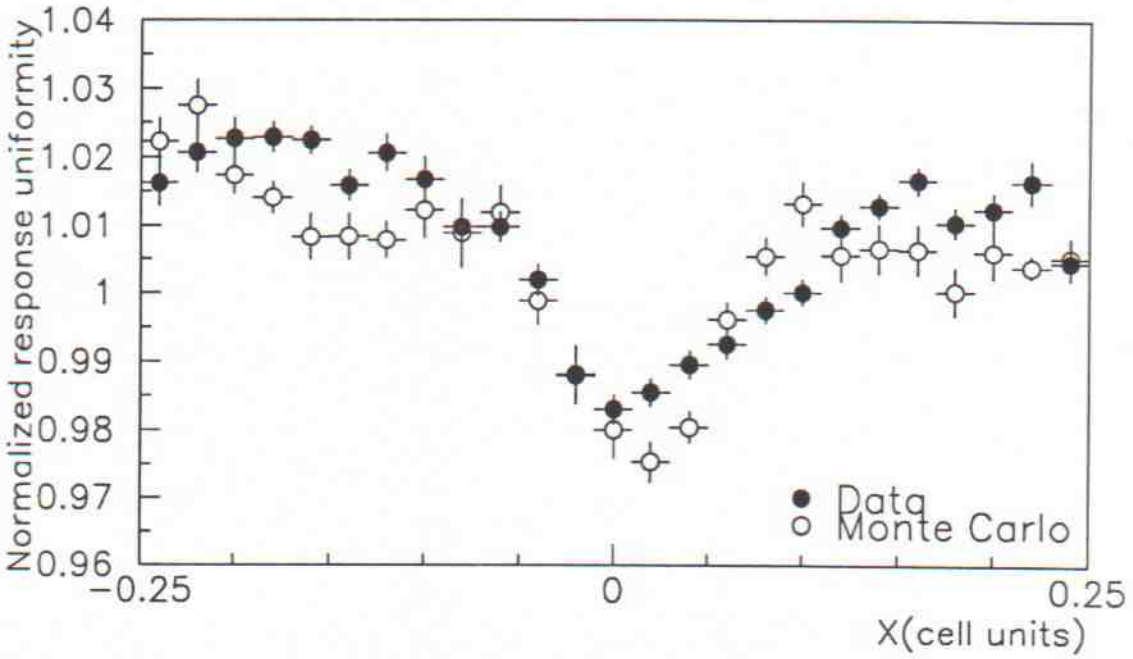

Figure 27: As for Fig. 19 but for the compensated geometry.

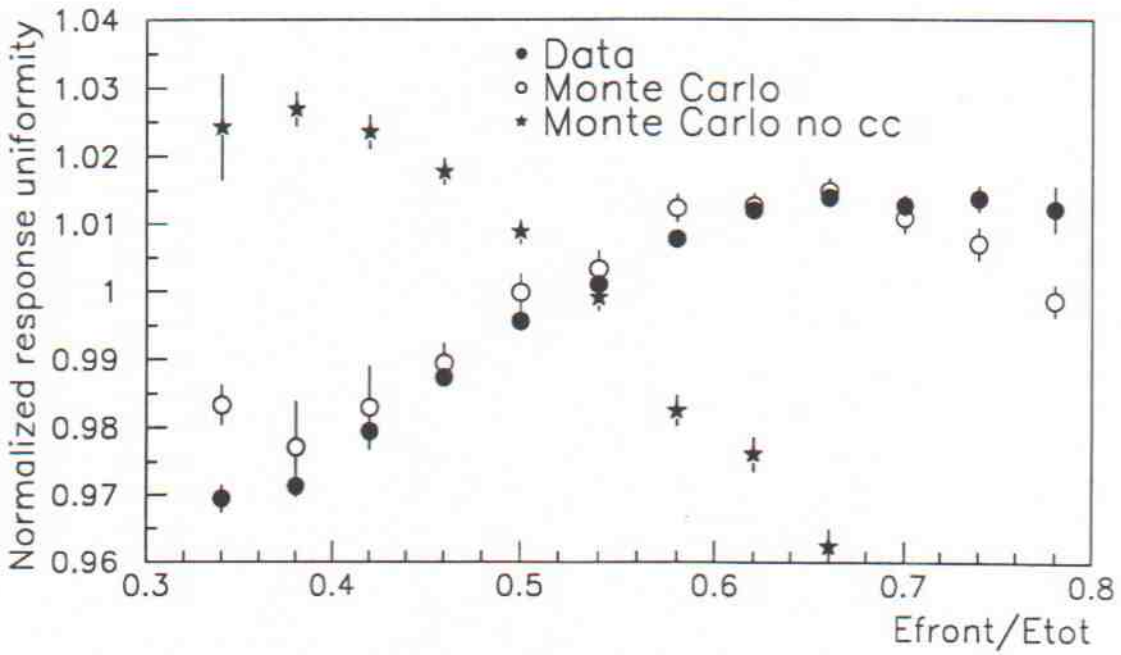

Figure 28: Variation of the energy response of the opening geometry calorimeter normalized to the beam energy for 90 GeV electrons as a function of the ratio of the energy in the front compartment to the total. Black stars show the simulation for a full charge integration (no convolution with electronic response).

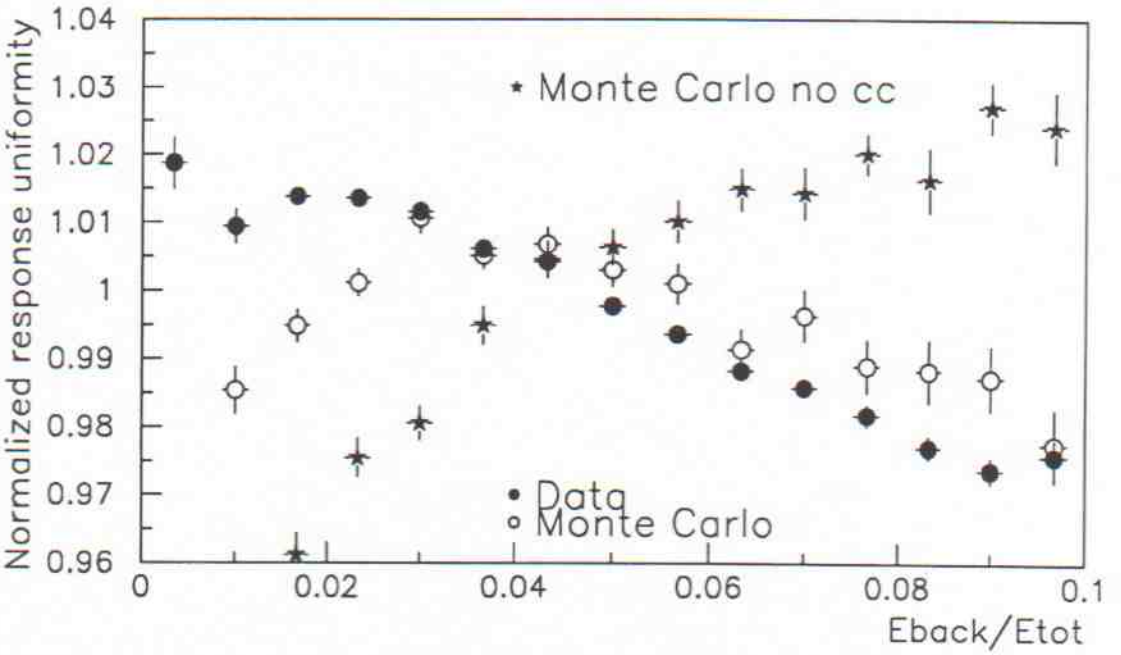

Figure 29: As for Fig. 21 but for the back compartment.

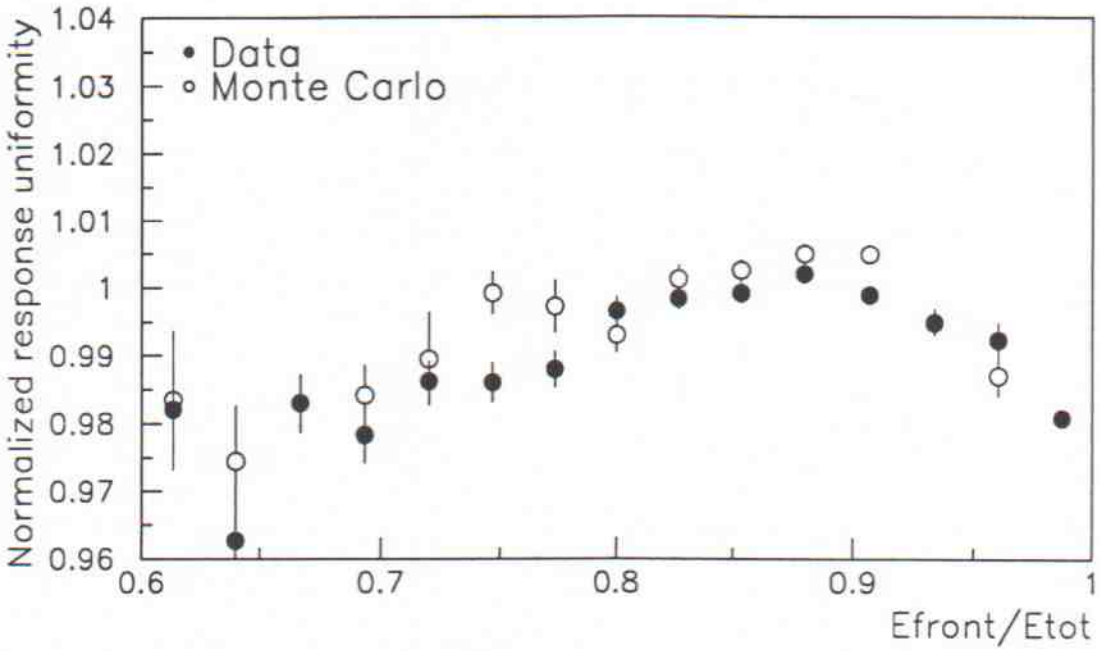

Figure 30: Variation of the energy response of the compensated geometry normalized to the beam energy for 90 GeV electrons as a function of the ratio of the energy in the front compartment to the total. In that case, both simulations with and without electronic response convolution should give the same result as the argon gap remains constant.

6 Pointing Geometry (1992 Prototype)

In this chapter, the simulated pointing geometry will be presented, Clearly, most of our simulation efforts are now on this geometry and work is in progress. Results will be presented in a subsequent note.

6.1 Geometry

6.1.1 analytical method

The pointing geometry is obtained by requiring that the thickness of the LAr gaps and of the absorber sheets be constant. This is achieved by varying the angle of the accordion folds along the depth of the calorimeter (see Fig. 31).

The parameters of such an accordion geometry can be obtained by first considering the family of curves separated by a distance (measured perpendicular to the tangent at one point) independent of ρ, the polar radius from the origin. Two such curves are shown below, starting at an inner radius $\rho_\circ$ and separated by a rotation of angle β about the origin O.

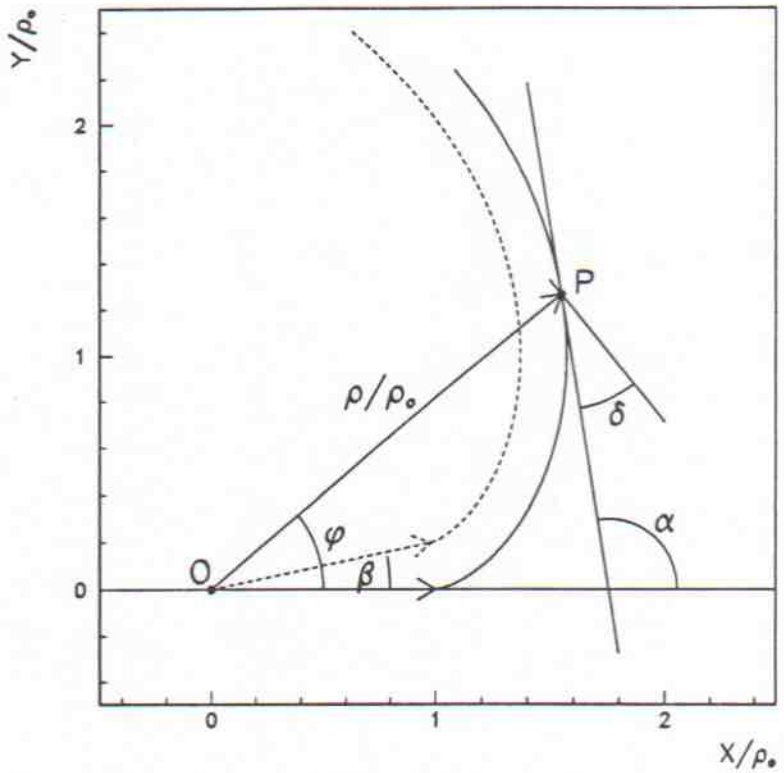

In general, the polar coordinate representation of any curve can be expressed in the form

$$\rho\frac{d\phi}{d\rho} = \tan(\alpha - \phi) = \cot\delta \tag{9}$$

where $\phi = \phi(\rho)$ is the azimuthal angle coordinate of point P, ρ is its polar radius coordinate, α is the azimuthal angle of the curve's tangent at point P, and δ is the angle between the tangent and the ϕ-axis at point P.

For small angular rotation β between two such curves, the distance separating them at point P is given by

$$\varepsilon = \beta\rho\sin\delta = \beta\rho_\circ \tag{10}$$

Requiring ε to be a constant creates a relation between ρ and δ which allows to obtain the function $\phi(\rho)$ desired. Differentiating equation 10 gives

$$\frac{1}{\rho}\frac{d\rho}{d\delta} = -\cot\delta$$

which can be used along with equation 9 to obtain

$$\frac{d\phi}{d\delta} = \left(\rho\frac{d\phi}{d\rho}\right)\left(\frac{1}{\rho}\frac{d\rho}{d\delta}\right) = -\cot^2\delta$$

with the solution, satisfying $\phi = 0$ at $\delta = \pi/2$ (or $\rho = \rho_\circ$),

$$\phi = \cot\delta + \delta - \frac{\pi}{2}.$$

From equation 10 we obtain

$$\cot\delta = \sqrt{\left(\frac{\rho}{\rho_\circ}\right)^2 - 1}$$

which finally gives

$$\phi(\rho) = \sqrt{\left(\frac{\rho}{\rho_\circ}\right)^2 - 1} - \arccos\left(\frac{\rho_\circ}{\rho}\right). \tag{11}$$

The radius of curvature of this curve, $R(\rho)$, can be obtained from

$$R = \frac{(\rho^2 + \rho'^2)^{3/2}}{\rho^2 + 2\rho'^2 - \rho\rho''}$$

where

$$\rho' \equiv \frac{d\rho}{d\phi} = \frac{\rho}{\sqrt{\left(\frac{\rho}{\rho_\circ}\right)^2 - 1}}$$

$$\rho'' \equiv \frac{d^2\rho}{d\phi^2} = -\frac{\rho}{\left[\left(\frac{\rho}{\rho_\circ}\right)^2 - 1\right]^2}.$$

We then obtain

$$R(\rho) = \sqrt{\rho^2 - \rho_\circ{}^2}.$$

These results were first presented by O. Gildemeister [10].

To produce an absorber sheet with the pointing accordion structure, the curve obtained from equation 11 is associated to the mid thickness or neutral fibre of the absorber sheet and is folded over at various ϕ values.

The pointing geometry is obtained by requiring the outside of the absorber sheet to be tangent to a ϕ-wedge of a given opening angle (this constraint allows also the fabrication of absorber sheets that can rest on all corners when put on a flat surface), taking into account that the folds are arcs of circle with a given radius of curvature.

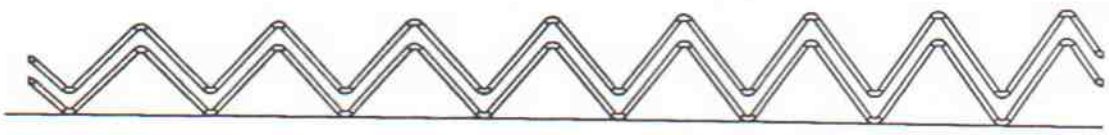

In the case of the EM accordion, the length of the curve between the folds is small and is approximated by a straight line (this causes a slightly variable gap – $\pm 1\%$ – along each fold). Note that this approximation is not valid in the case of the hadronic accordion calorimeter.

The geometrical parameters of the absorber sheets are then determined by

- the opening angle of the ϕ-wedge containing the sheet;
- the number of absorber sheets in a full circle ($2\pi/\beta$);
- the gap width between the neutral fibre of two adjacent absorber sheets (ε);
- the absorber thickness;
- the radius of curvature of the absorber sheet corners;
- the inner radius (ρ_o).

The electrode sheets are then produced using the same neutral fibre curve.

The optimisation of these parameters is obtained by requiring that the thickness of LAr traversed radially shows best uniformity in ϕ.

The geometrical parameters corresponding to the 1992 pointing accordion prototype absorber sheets are shown in table 6, where (ρ_C, ϕ_C) are the coordinates of the center of curvature of the accordion corners, ξ is the angle in the corners, ρ_m are the polar radius coordinates of the neutral fibre of the sheets at $\phi = 0$, and Σ is the accumulated developped length of the neutral fibre of the sheets.

Figures 32 and 33 show the corresponding LAr and total radiation length for normal incidence (at $\eta = 0$) as a function of ϕ of impact, which are found to be of very similar shape as for the cartesian geometry.

6.1.2 iterative method

From another point of view the problem of a constant gap is directly settled as follows: try to define an accordion structure inside a cone (pointing geometry) with the following characteristics:

- The curvature centre for the neutral fibre C_1 is known for the corner 1.
- The radius of curvature is fixed ($r_0 = 3$ mm here).
- The next foil (F') is deduced from (F) by a plane rotation $\mathcal{R}(O, \beta)$.

At this level, there remains one degree of freedom for determining the next curvature centre C_2: for example the angle δ_1 of the neutral fibre with respect to the direction of the outside bisector N.

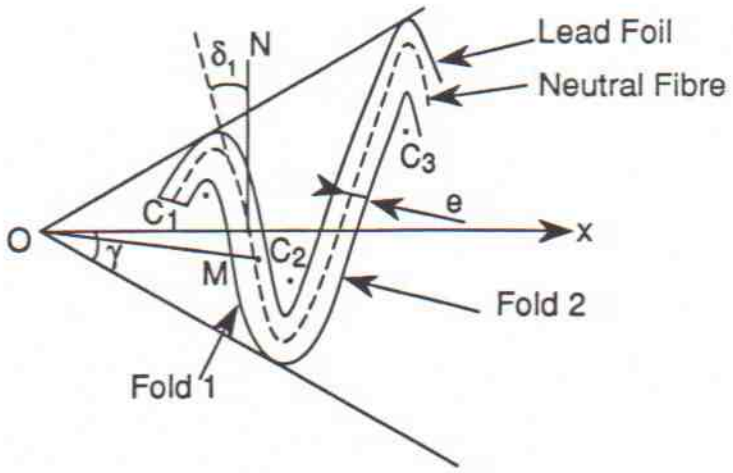

A constraint, such as a constant gap between the two foils (F) and (F'), fixes this parameter. In fact, as pointed out previously, the gap is not exactly constant in the case of straight lines joining the corners. So, one has to choose the point M along the fold where the gap value is put at a fixed value. Obviously such a point is chosen with the same geometrical definition for every next fold.

Then, if $\rho_M(\delta_1)$ and $\varphi_M(\delta_1)$ are the polar coordinates of M in the fold 1, the constraint is written as:

$$f\,[\rho_M(\delta_1),\ \varphi_M(\delta_1)] = 0 \Longleftrightarrow F(\delta_1) = 0\ .$$

This last equation is solved to get δ_1. Then one gets the curvature centre $C_2(\rho_2$ and $\varphi_2)$. A new point M (in between C_2 and C_3) is used in the same way and the constraint yields the parameter δ_2 for the fold 2. The total accordion structure is obtained by iteration.

This iterative method exhibits a priori two advantages:

a) It is possible to vary the geometrical definition of the auxiliary point M to minimize the gap variation along folds.

b) It is easy to impose another type of constraint such as 'radial gap thickness is constant'; again this can be put in mean only along a given fold (for example, this constraint is written in the vicinity of the bisector O_x).

Concerning the first point, it turns out that the best choice for M is the middle of the fold (i.e. slightly above or below the bisector according to the slope sign of the fold). The corresponding set of δ angles which define the fold positions is then exactly the one obtained with the analytical method described above. (By the way, the iterative method specifies the place along the folds where the constant value for the gap is imposed and maintained with the approximation of a gap with a null curvature.)

Concerning the second point (b), taking into account the fact that the direction of particles in a shower is rather in a radial direction than systematically perpendicular with respect to each successive electrode, one can try to investigate a new folding with a constraint on the radial thickness in LAr. The iterative method yields in this case a new set of δ angles which can be used in comparative simulation methods.

illustration of the iterative method Consider the expression of the constraint at the level of a given n-fold between the two curvature centres C_n and C_{n+1}. The O_x axis is the bisector of the cone containing a folded foil. As explained above, for a chosen M point, its polar coordinates are functions of the angle δ_n : $\rho_M(\delta_n)$ and $\varphi_M(\delta_n)$.

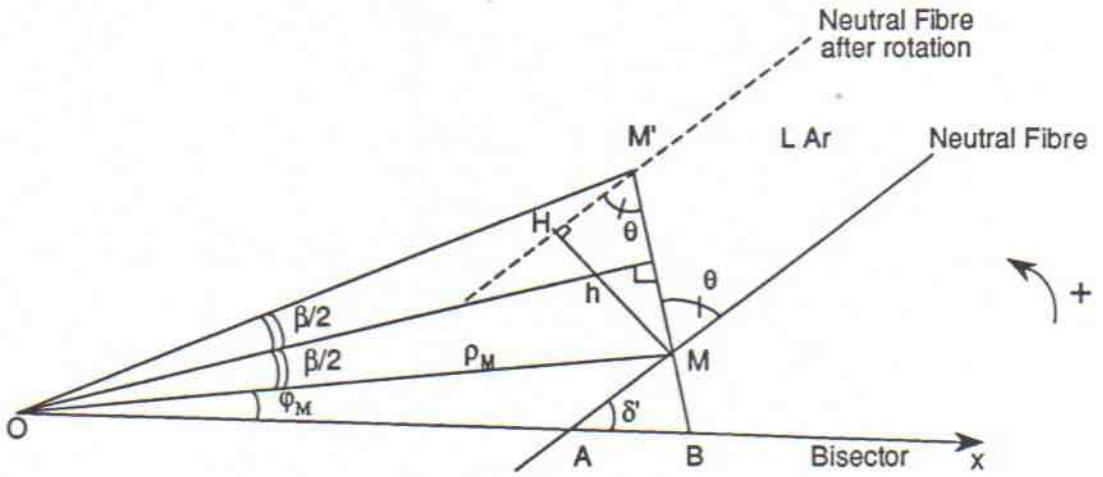

The rotation $\mathcal{R}(O,\ \beta)$ of the neutral fibre of a foil defines a LAr cell and (MM′) are corresponding points. As a constraint one writes (case of a constant gap here):

$$MH = MM'\sin\theta = h, \text{ where } h \text{ is a given constant.}$$

From very simple geometry, MM′ and θ can be expressed using the known parameters and the δ_n angle. Let $\delta' = \pi/2 - \delta_n$, then:

- $MM' = 2\rho_M \sin\beta/2$
- θ calculation:

$$\begin{aligned}
\hat{B} &= \frac{\pi}{2} - (\varphi_M + \beta/2) \\
\theta &= \widehat{AMB} = \pi - (\hat{B} + \delta') = \frac{\pi}{2} - \delta' + \varphi_M + \beta/2 \\
\theta &= \delta_n + \varphi_M + \beta/2
\end{aligned}$$

So the constraint equation is:

$$2\rho_M(\delta_n)\sin\beta/2\,\sin(\delta_n + \varphi_M(\delta_n) + \beta/2) = h\ .$$

This equation yields δ_n which is determined very quickly by dichotomy.

Remark: The exact expressions for $\rho_M(\delta_n)$ and $\varphi_M(\delta_n)$ depend on the choice for the M position. And, in the same way, one has to take care of the exact position of M with respect to the intersection A of the bisector O_x with each fold. For example, if M is the middle of the fold, it is above (below) A for a fold with positive (negative) slope. For various possible choices of M (as explained at the end of 6.1.2), this is taken into account in detail in the previous calculation of θ.

6.1.3 pseudorapidity structure

The absorber sheets making the 1992 pointing prototype are made of a total thickness of 1.8 mm of lead, 0.2 mm of glue and 0.4 mm of stainless steel for $\eta < 0.7065$. For bigger η, the composition is then 1.2 mm of lead, 0.4 mm of glue and 0.8 mm of stainless steel, adding up to the same geometrical thickness of 2.4 mm but with a smaller radiation length thickness. This choice is meant to help recover a good energy resolution at high η.

Figure 34 shows the total radiation length seen from the vertex as a function of the pseudorapidity. The cloud of points at a given η are produced by a uniform distribution in ϕ (see Fig. 33 for the $\eta = 0$ case). The discontinuity at $\eta = 0.7065$ is clearly seen.

6.2 Note on the Coding of the Pointing Geometry

In GEANT, a complex volume can often be simply represented if there exists a symmetry leading to repetition of parts of the volume, as in the case of a cube made up of smaller identical cubes, or a cylinder made up of identical ϕ or ρ slices. In the case of the accordion with pointing geometry, the ϕ symmetry that exists cannot be used in the current versions of GEANT. Furthermore, no structures can be repeated in ρ since the accordion angle varies with ρ. No repetitions are present in η either.

Therefore, in the case of the accordion, a conventional use of GEANT leads to the creation of a large mother volume filled with LAr in which every daughter volumes making all the absorber and electrode sheets (18 corners and 17 straight sections each!) have to be positioned. This results in a mother volume filled with thousands of daughter volumes and directly leads to a very slow volume search by the GEANT tracking.

Another problem arises when we want the LAr gap number in which a hit is produced (to associate the hit to a given cell). Since a hit in the LAr is in the mother volume, GEANT does not know which gap this corresponds to.

These two problems were solved using rather obscure GEANT features, thanks to comments and advice from Michel Maire [11].

6.2.1 GSUNEA and GUNEAR

The slow tracking of GEANT in the case of a mother volume containing a large number of daughters comes from the fact that each time GEANT requires to know in which daughter it is or will be tracking, it searches systematically through the whole list of daughter volumes.

Clearly, at any step of tracking, the coordinates and direction cosines of the current tracking step is known. From this and the knowledge of the geometry, a restricted list of candidate daughter volumes to be searched for can be built. GEANT can then be instructed to search only through that list, speeding up considerably the execution of the code. This can be done with the use of the routine GSUNEA and GUNEAR in the following way:

- At initialisation phase, you must tell GEANT that you want to use a user volume search for the volume, say, CALO:

```
      ISEARC=1  ! could be any number>0. User defined, associated to CALO
      CALL GSUNEA('CALO',ISEARC)
```

- Then you must provide GEANT with a user search routine. It must have the following format:

```
      SUBROUTINE GUNEAR(ISEARC,ICALL,X,JNEAR)
C
C   ************************************************************************
C   *                                                                      *
C   *  produce a list of volumes to search for when in volume ISEARC       *
C   *                                                                      *
C   *  input                                                               *
C   *                                                                      *
C   *  ISEARC  number associated to the volume in which the user           *
C   *          search is used (set by user with GSUNEA)                    *
C   *  ICALL   type of question the list of volumes must answer            *
C   *          1 -->  GMEDIA like call (where am I?)                       *
C   *          2 -->  GNEXT  like call (where can I go?)                   *
C   *  X       X(1),X(2),X(3)   position                                   *
C   *          X(4),X(5),X(6)   direction cosines                          *
C   *  JNEAR   Pointer to the volume list bank                             *
C   *          The list of volumes to search to answer the question        *
C   *          defined by ICALL contains the numbers corresponding         *
C   *          to the volumes to search, the first in the list will        *
C   *          be search first.  These volume numbers correspond to        *
C   *          the rank of position (GSPOS) of the daughter volumes        *
C   *          in the mother volume associated to ISEARC (it is in         *
C   *          fact the link number of the daughter volume bank).          *
C   *          The list of volumes must be entered as follows:             *
C   *                                                                      *
C   *          IQ(JNEAR+1) = N   number of volumes in the list             *
C   *          IQ(JNEAR+1+1) = volume number of the 1st volume in list     *
C   *          IQ(JNEAR+1+2) = volume number of the 2nd volume in list     *
C   *              ...                                                     *
C   *          IQ(JNEAR+1+N) = volume number of the Nth volume in list     *
C   *                                                                      *
C   * *** WARNING ***                                                     *
C   * Using GUNEAR bypasses GEANT volume search.  Your user search is     *
C   * your responsability.  If the list of volumes to search you give     *
C   * is incomplete, you will obtain wrong results without warning...     *
C   * The rightness of your algorithm can be verified by checking that    *
C   * the seed number after the simulation of a shower is the same        *
C   * with and without the user search.                                   *
C   *                                                                      *
C   * *** DISCLAIMER !! ***                                               *
```

```
C   * As far as I know, this is not documented anywhere.              *
C   * I have not heard of anybody using GUNEAR.                       *
C   * My understanding of this routine might not be completely correct.*
C   *                                                                 *
C   * The existence of this routine was mentioned to me by Michel     *
C   * Maire... many thanks.                                           *
C   *                                                                 *
C   * Michel Lefebvre    March 1992                                   *
C   *                                                                 *
C   *******************************************************************
C
C make sure you have the GEANT common block with IQ array...
+SEQ,GCBANK.
C
      INTEGER MYLIST(100)
C
C here make a list of volume numbers using ISEARC, ICALL, X
C remember this routine will be called VERY often
C
      N = ...
      MYLIST(1 to N) = .....
C
C stuff GEANT with it
C
      DO 10 I=1,N
        IQ(JNEAR+1+I)=MYLIST(I)
 10   CONTINUE
      IQ(JNEAR+1)=N
C
      END
```

6.2.2 UPWGHT in COMMON/GCTRAK/

The LAr gap number associated to a hit (needed to associate hits to a given accordion cell) can in principle be obtained, at any tracking step, from the coordinates of the step in the LAr mother volume. This leads to a rather complicated mathematical treatment due to the nontrivial accordion structure.

A solution consists in making use of the number of a daughter volume exited by the tracking of a particle. During tracking, in subroutine GUSTEP when a particle leaves an absorber or an electrode volume, the corresponding daugher volume number (along with the direction cosines or the coordinates in the case of absorber only) easily provides the LAr gap number where the tracking will now proceed.

If no interactions were to occur in the LAr gap, this gap number could be stored in a user variable and used when energy is deposited in a subsequent step. Since interactions do occur in LAr, the tracking can branch off. The gap number would then be lost when tracking resumes at that point.

An elegant solution to this problem consists in storing the LAr gap number obtained on exit of a daughter volume in the user word UPWGHT in COMMON/GCTRAK/. If the tracking branches off, the LAr gap number (along with the tracking parameters) is pushed down the particle stack. When energy is deposited in a subsequent step, the COMMON/GCTRAK/ is refreshed by GEANT from the particle stack, with the appropriate LAr gap number in UPWGHT.

Opening angle of ϕ-wedge containing the sheet (degrees)	1.160
Number of absorber sheets in a full circle ($2\pi/\beta$)	960
Gap width between the neutral fibre of two adjacent sheets (cm)	0.66
Absorber sheet thickness (cm)	0.24
Radius of curvature of the absorber sheet corners (cm)	0.3
Inner radius (cm)	134.85

	ρ_C (cm)	ϕ_C (degrees)	ξ (degrees)	ρ_m (cm)	Σ (cm)
0	134.85	-0.128		134.85	0.000
1	136.50	-0.404	95.292	137.97	2.110
2	139.47	0.407	92.632	140.91	6.065
3	142.39	-0.411	90.194	143.81	10.025
4	145.27	0.414	87.935	146.67	13.996
5	148.11	-0.418	85.830	149.50	17.984
6	150.92	0.421	83.860	152.30	21.992
7	153.71	-0.423	82.008	155.07	26.024
8	156.46	0.426	80.263	157.81	30.082
9	159.20	-0.429	78.611	160.54	34.168
10	161.92	0.431	77.045	163.25	38.285
11	164.61	-0.434	75.556	165.94	42.433
12	167.30	0.436	74.138	168.62	46.615
13	169.97	-0.438	72.784	171.28	50.832
14	172.62	0.441	71.490	173.93	55.084
15	175.27	-0.443	70.250	176.57	59.373
16	177.90	0.445	69.088	179.36	63.699
17	179.36	-0.096			65.998

Table 6: 1992 pointing prototype geometrical parameters. See text.

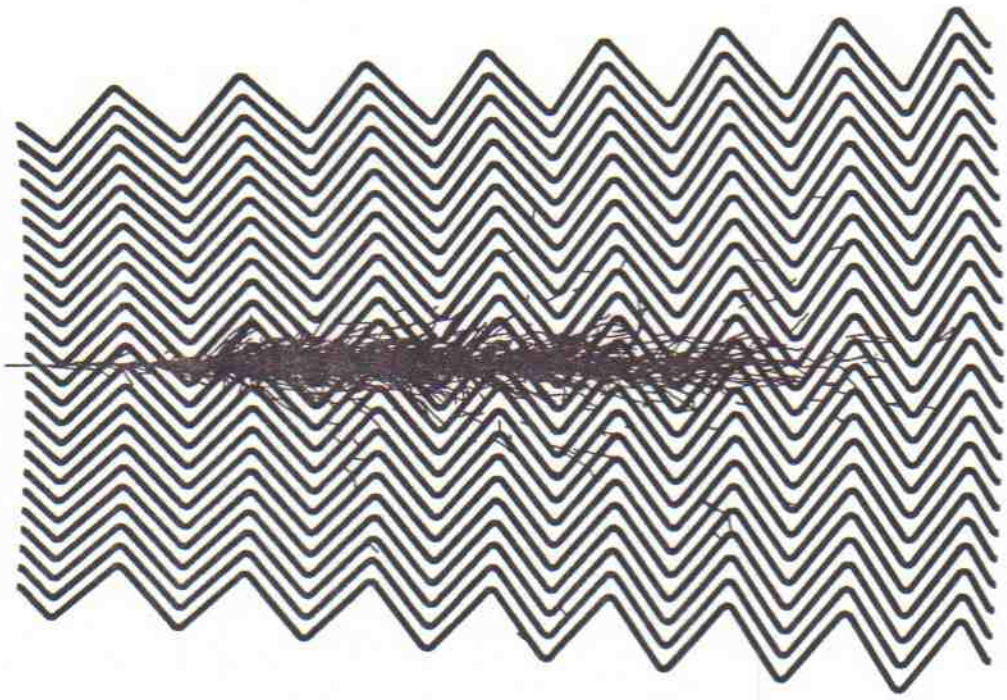

Figure 31: Section of the simulated pointing geometry. Note that the accordion angles vary in order to keep the LAr gap constant. A 100 GeV electron shower is also simulated. Only absorber sheets and charged tracks down to 10 MeV are shown.

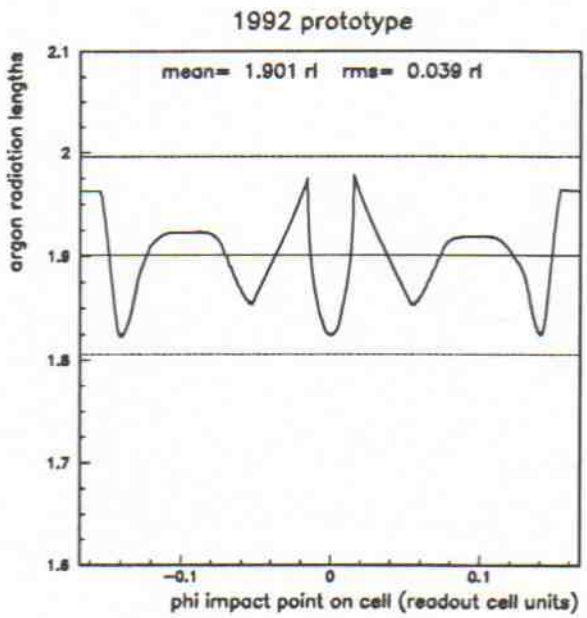

Figure 32: LAr thickness traversed (at $\eta = 0$), in radiation length, as a function of ϕ in cell units (since one cell is made of 3 absorber sheets, the span here is $\pm 1/6$ between two adjacent sheets). The dotted lines show a $\pm 5\%$ band.

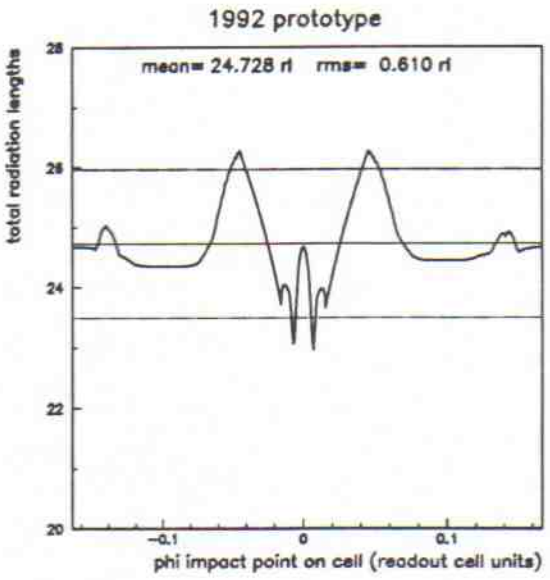

Figure 33: Total thickness traversed (at $\eta = 0$), in radiation length, as a function of ϕ in cell units (since one cell is made of 3 absorber sheets, the span here is $\pm 1/6$ between two adjacent sheets). The dotted lines show a $\pm 5\%$ band.

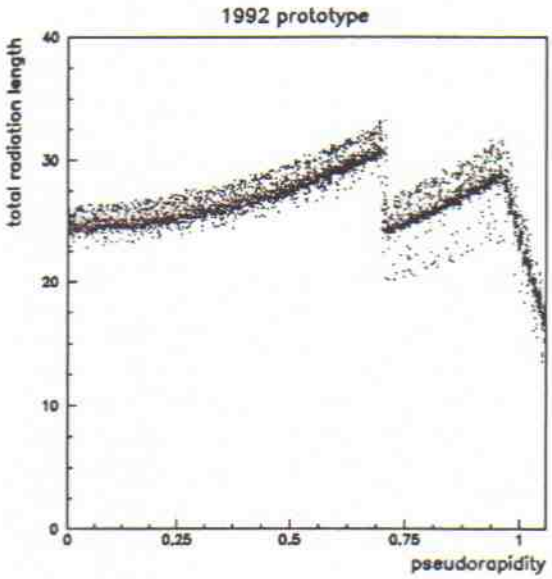

Figure 34: Total radiation length seen from the vertex of the pointing prototype (in the case of a colliding been setup) as a function of the pseudorapidity η. The many points at a given η are produced by a uniform distribution in ϕ. The η range covers the part of the prototype equipped with readout cells. The discontinuity at $\eta = 0.7065$ caused by a change in the absorber material composition is clearly seen.

7 Last Remark and Acknowledgements

A summary of results from GEANT simulation of the 1990 (cartesian) and 1991 (cylindrical) EM accordion calorimeter prototype is presented in this note, including detailled simulation of the charge drift and collection. Comparison with experimental data is also presented in many cases.

The geometry of the 1992 (pointing) EM accordion calorimeter prototype is described. Simulation efforts are now in progress and the results will be part of a subsequent note.

Comments on this note would be appreciated (they can be sent to LFB@CERNVM).

The authors would like to thank Guy Le Meur (LAL, Orsay) and Michel Maire (LAPP, Annecy) for their very helpful contributions.

References

[1] B. Aubert et al. (RD3 Collaboration), *CERN/DRDC/***90–31** (1990) and *CERN/DRDC/***91–21** (1991), *DRDC/***P5–Add.1**.

[2] B. Aubert et al. (RD3 Collaboration), *Nucl. Inst. and Meth.* **A309** (1991) 438-449.

[3] B. Aubert et al. (RD3 Collaboration), *Nucl. Inst. and Meth.* **A321** (1992) 467-478.

[4] B. Aubert et al. (RD3 Collaboration), *CERN-PPE/***92–129** (1992), submitted to *Nucl. Inst. and Meth.*

[5] M. Lefebvre, M. Pepe and G. Polesello, ATLAS internal note CAL-NO-**002**, 24 May 1990.

[6] J. Feltesse, DPh PE CEN-Saclay. Proc., Vienna 1989.

[7] L. Onsager, Phys. Rev. **54** (1938) 554.

[8] D.C. Rahm, B.N.L. Private Communication.

[9] G. Le Meur, A Mixed Finite Element Method for Particle Simulation in Lasertron, LAL-RT **87-01**, March 1987.

[10] O. Gildemeister, CERN, private communication in the Atlas RD3 group.

[11] M. Maire, LAPP Annecy, private communication.